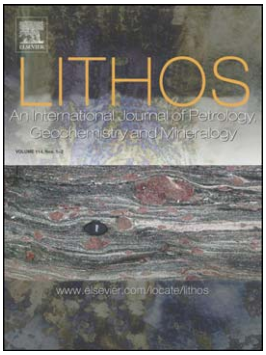

Incremental growth of an upper crustal, A-type pluton, Argentina: Evidence of a re-used magma pathway

Pablo H. Alasino, Mariano A. Larrovere, Sebastián Rocher, Juan A. Dahlquist, Miguel A.S. Basei, Valbone Memeti, Scott Paterson, Carmen Galindo, Marcos Macchioli Grande, Mario da Costa Campos Neto

PII: S0024-4937(17)30151-2
DOI: doi:10.1016/j.lithos.2017.04.013
Reference: LITHOS 4294

To appear in: *LITHOS*

Received date: 21 November 2016
Accepted date: 12 April 2017

Please cite this article as: Alasino, Pablo H., Larrovere, Mariano A., Rocher, Sebastián, Dahlquist, Juan A., Basei, Miguel A.S., Memeti, Valbone, Paterson, Scott, Galindo, Carmen, Grande, Marcos Macchioli, da Costa Campos Neto, Mario, Incremental growth of an upper crustal, A-type pluton, Argentina: Evidence of a re-used magma pathway, *LITHOS* (2017), doi:10.1016/j.lithos.2017.04.013

Incremental growth of an upper crustal, A-type pluton, Argentina: evidence of a re-used magma pathway

Pablo H. Alasino[1-2*], Mariano A. Larrovere[1-2], Sebastián Rocher[1], Juan A. Dahlquist[3], Miguel A.S. Basei[4], Valbone Memeti[5], Scott Paterson[6], Carmen Galindo[7], Marcos Macchioli Grande[1-2] and Mario da Costa Campos Neto[4]

[1]Centro Regional de Investigaciones Científicas y Transferencia Tecnológica de La Rioja (Prov. de La Rioja-UNLaR-SEGEMAR-UNCa-CONICET), Entre Ríos y Mendoza s/n, Anillaco, 5301, Argentina.
[2]Instituto de Geología y Recursos Naturales, Centro de Investigación e Innovación Tecnológica, Universidad Nacional de La Rioja (INGeReN-CENIIT-UNLaR), Av. Gob. Vernet y Apóstol Felipe, 5300, La Rioja, Argentina.
[3]Centro de Investigación en Ciencias de la Tierra (CICTERRA-CONICET-UNC), Av. Vélez Sarsfield 1611, Pab. Geol., X5016CGA Córdoba, Argentina.
[4]Instituto de Geociências da Universidade de São Paulo, RAU do Lago, 562, São Paulo, SP 05508-080, Brazil.
[5]Departament of Geological Sciences, California State University Fullerton, CA 92831, USA.
[6]Department of Earth Sciences, University of Southern California, Los Angeles, CA 90089, USA.
[7]Departamento de Petrología y Geoquímica, Universidad Complutense, Instituto de Geociencias (CSIC-UCM), 28040 Madrid, Spain.

*Corresponding author. *E-mail address*: palasino@crilar-conicet.gob.ar

ABSTRACT

Carboniferous igneous activity in the Sierra de Velasco (NW Argentina) led to the emplacement of several magmas bodies at shallow levels (< 2 kbar). One of these, the San Blas intrusive complex formed over millions of years (≤ 2-3 m.y.) through three periods of magma additions that are characterized by variations in magma sources and emplacement style. The main units, mostly felsic granitoids, have U-Pb zircon crystallization ages within the error range. From older to younger (based on cross-cutting relationships) intrusive units are: (1) the Asha unit (340 ± 7 Ma): a tabular to funnel-shaped intrusion emplaced during a regional strain field dominated by ~WSW-ENE shortening with contacts discordant to regional host-rock structures; (2) the San Blas unit (344 ± 2 Ma): an approximate cylindrical-shaped intrusion formed by multiple batches of magmas, with a roughly concentric fabric pattern and displacement of the host rock by ductile flow of about 35 % of shortening; and (3) the Hualco unit (346 ± 6 Ma): a small body with a possible mushroom geometry and contacts concordant to regional host-rock structures. The magma pulses making up these units, define two groups of A-type granitoids. The first group includes the peraluminous granitic rocks of the Asha unit generated mostly by crustal sources

(εNd_t = −5.8 and εHf_t in zircon = −2.9 to −4.5). The second group comprises the metaluminous to peraluminous granitic rocks of the youngest units (San Blas and Hualco), which were formed by a heterogeneous mixture between mantle and crustal sources (εNd_t = +0.6 to –4.8 and εHf_t in zircon = +3 to −6). Our results provide a comprehensive view of the evolution of an intrusive complex formed from multiple non-consanguineous magma intrusions that utilized the same magmatic plumbing system during downward transfer of host materials. As the plutonic system matures, the ascent of magmas is governed by the visco-elastic flow of host rock that for younger batches include older hot magma mush. The latter results in ductile downward flow of older, during rise of younger magma. Such complexes may reflect the plutonic portion of volcanic centers where chemically distinct magmas are erupted.

Keywords: emplacement; A-type granite; nested intrusions; upper crust; Sierra de Velasco

1. Introduction

The ascent of silicic magmas from lower crustal depths and its emplacement in the upper crust is a poorly understood mass and heat transfer process (e.g., Read, 1962; Petford et al., 2000). Silicic magmas stored at shallow crustal levels form pluton, dike and/or sill complexes, and when the conditions are appropriate, feed volcanic eruptions. Studies of volcano-plutonic systems reveal that the plutons (at a depth of more than 5 km) associated with rhyolitic volcanism appear to have distinct felsic upper parts (~12 km thick at Taupo and ~15 km at Yellowstone) and mafic lower parts (e.g., Wilson and Charlier, 2016 and reference therein). The structure of the felsic upper parts will depend on the thermal and mechanical maturation of the crust in response to the mantle power input (e.g., Yoshinobu et al., 1998; de Silva et al., 2006; Karlstrom et al., 2009; Cao et al., 2016). Discrete plutons mostly disconnected from their source form under a normal arc geothermal gradient, but when intrusion occurs episodically through time the effects of a continuous addition of heat to the upper crust will

form a thermally complex magma transfer zone, or plumbing system, from the source region that evolves over time (e.g., Yoshinobu et al., 1998; Paterson et al., 2016).

Recent numerical modeling using variable crustal geothermal gradients shows the potential for a complex interplay between diking and diapirsm to facilitate magma ascent and emplacement into the middle and upper crust (e.g., Cao et al., 2016). In such a model, magma cannot penetrate the cold upper crust without frequent, multiple magma injections, as single magma bodies solidify too quickly to ascend over long distances (Miller and Paterson 2001; Cao et al., 2016). This implies that it may be common for multiple, potentially even unrelated magmas to use the same ascent pathway leading to magma mixing, host rock assimilation and recycling, playing important roles in the complex structural and compositional evolution of these magmas and resulting plutons (e.g., Saleeby et al., 1990; Paterson and Vernon, 1995; Miller and Paterson, 2001; Paterson and Farris, 2008; Miller et al., 2007; Davidson et al., 2007; Gasching et al., 2016; Paterson et al., 2016). These observations raise the 'room problem' in a growing magma chamber, particularly how younger batches displace older intrusive materials in an environment that in terms of temperature and rate of intrusion can evolve over time. Attempting to address the detailed evolution of magmatic plumbing systems requires a comprehensive study of (i) the geometry of magma bodies, (ii) multiple magmatic fabrics in each magma batch to identify increments of strain, (iii) timescales and emplacement modes of the intrusions, and (iv) petrogenesis of magma batches. One plutonic system where such studies have been completed is the Carboniferous A-type San Blas intrusive complex formed in the Eastern Sierras Pampeanas, NW Argentina. This intrusive complex consists of silica-rich granitoids associated with mafic dikes generated in a retro-arc region, formed contemporaneously with I-type granites to the west (e.g., Alasino et al., 2012).

The aim of this paper is to explore the structure and composition of the San Blas, a well-exposed, upper crustal plutonic complex in the northern part of the Sierra de Velasco (**Fig. 1**) that formed from nesting of multiple, successive A-type intrusions at a depth of about 5 km. We present a comprehensive data set including field observations, structural data, whole-rock element geochemistry, whole rock and mineral scale Sr-Nd-Pb-Hf isotope compositions, and U-Pb zircon geochronology from three intrusive units forming the San Blas intrusive complex. Our results provide a complete geologic record of the evolution of the three intrusive units that reflect the nesting of unrelated batches of magmas at shallow crustal levels. We document the incremental growth of shallow magma chambers by the re-use of the same ascent pathway by distinct magmas, which may reflect the plutonic source that feeds volcanic centers where chemically distinct magmas are erupted (Bachmann and Bergantz 2004; Hildreth 2004; Farina et al., 2010; Wilson and Charlier, 2016).

2. Geological setting

2.1. Sierras Pampeanas

The proto-Andean margin of Gondwana was an active accretionary orogen from at least the Cambrian until the present (Cawood, 2005) and experienced a number of magmatic flare-ups. Part of this history is preserved in the Sierras Pampeanas of NW Argentina (26°−32°S) (**Fig. 1a**), now exposed by tilting caused by the Andean compression since the Miocene (e.g., Jordan and Allmendinger, 1986). Geochronological data show that four main magmatic events took place in the Sierras Pampeanas in the Paleozoic: a) Early Cambrian (Pampean orogeny), b) Ordovician (Famatinian orogeny), c) Middle–Late Devonian magmatism (Achalian orogeny) and d) Carboniferous (e.g., Pankhurst and Rapela, 1998; Vaughan and

Pankhurst, 2008 and references therein). After the Devonian intracontinental magmatism (ca 390–365 Ma), which involved an important amount of reworking of supracrustal material, Carboniferous magmatism (ca. 310–355 Ma) occurred along more than 1000 km in the Sierras Pampeanas, southern Puna and Cordillera Frontal exhibiting temporal and geochemical variations (Alasino et al., 2012; Dahlquist et al., 2013; Coira et al., 2016). Farther inland (i.e., Eastern Sierras Pampeanas, **Fig. 1a**) the resulting plutons have a distinct A-type geochemical signature with participation of both juvenile mantle material and continental crust (Dahlquist et al., 2010). To the west in the Western Sierras Pampeanas and Cordillera Frontal (**Fig. 1a**), the plutons show a calc-alkaline signature (Llambías and Sato, 1995; Gregori et al., 1996; Alasino et al., 2012).

The Carboniferous A-type magmatic flare-up in the Eastern Sierras Pampeanas is represented by scattered and undeformed plutons, usually sub-circular and associated with penecontemporaneous mafic dikes of trachybasalt and trachyandesite composition. This magmatism was emplaced in a retro-arc setting linked to an active magmatic arc to the west (Alasino et al., 2012). This mainly granitic magmatism intruded into rocks assigned to the Ordovician Famatinian orogeny (**Fig. 1**). Famatinian granitoid host rocks of the Sierra de Velasco often show evidence for sub-solidus ductile shearing (López and Toselli, 1993). This shear zone is composed of mylonites and protomylonites (~NNW-SSE strike) formed under amphibolite-facies conditions (**Fig. 1b**) (e.g., Rossi et al., 1999; Larrovere et al., 2016).

The Sierra de Velasco in the La Rioja province represents one of the best crustal sections to study the Late Devonian−Carboniferous A-type event (**Fig. 1b**). In the north-central Sierra de Velasco, most of the Carboniferous granitoids appear as discrete plutonic bodies called the Asha, San Blas, Huaco, La Chinchilla and Sanagasta plutons (Dahlquist et al., 2006, 2010; Grosse et al., 2009; Macchioli Grande et al., 2015). Strongly peraluminous granitoids

associated with this A-type event (e.g., La Costa pluton, Alasino et al., 2010) have magmatic Grt-Bt assemblages with estimated pressures of < 2 kbar, which suggests shallow emplacement.

2.2. Structure and composition of the northern Sierra de Velasco

The northern Sierra de Velasco is a well-exposed crustal block that was uplifted during Miocene to Holocene Andean tectonics by a reverse fault along its eastern side, resulting in a steep slope on this flank and a relatively gentle slope on the west side (**Fig. 2**). The smooth, western flank represents an ancient, regional-scale Pampean peneplain (Jordan et al., 1989). This basement block consists mostly of Carboniferous granitoids with excellent 3-D exposures. At the base of the western flank, Miocene continental strata rest unconformably on the crystalline basement. Both the unconformity and Miocene bedding are gently tilted (12-15 degrees) towards the NW suggesting that the current orientation of the block is only slightly tilted from its original orientation (**Fig. 2**).

New mapping in the northern part of the Sierra de Velasco established three main intrusive units, which together form the San Blas Intrusive Complex (SBIC) (**Fig. 3**). From oldest to youngest, these units are: (1) the Asha unit (AU); (2) the San Blas unit (SBU) and (3) the Hualco unit (HU). The AU has a porphyritic texture with a medium-grained matrix of plagioclase, microcline, quartz and biotite surrounding K-feldspar megacrysts (2-5 cm long and about 30 modal %). This unit was mapped in the northern part of the mountain range, covering ca. 320 km^2 of the western and eastern flanks (**Fig. 1b**). The ages obtained in the western and eastern flanks reveal different U-Pb zircon and monazite crystallization ages of 343 ± 1 Ma and 361 ± 4 Ma, respectively (Báez et al., 2004 and Toselli et al., 2011;

respectively), suggesting that the AU formed by more than one intrusion. The oldest age is derived from outside the study area near the town of Anillaco (**Fig. 1b**). We are reporting a new U-Pb zircon age for the AU from the western flank (see below) that is similar to that published by Baez et al. (2004).

The SBU is a semi-elliptical body with an outcrop area of approximately 120 km^2. The dominant rock type is porphyritic with large microcline crystals (3–15 cm long, constituting up to 40% of the mode), and ranges from a biotite-rich granodiorite or monzogranite to syenogranite in composition. The matrix is coarse- to medium-grained, equigranular, and composed of mainly quartz, microcline, plagioclase, and biotite. Internal contacts vary from sharp to gradational. Published ages for the SBU include a monazite U-Pb TIMS age of 334 ± 5 Ma (Báez et al., 2004) and a zircon U–Pb SHRIMP age of 340 ± 3 Ma (Dahlquist et al., 2006) (**Fig. 1b**). Below we present a new U-Pb zircon age for the SBU that is similar to the age determined by Dahlquist et al. (2006).

The HU intrudes the SBU and therefore is the youngest pulse in the northwestern region of the complex. The HU main body has an elliptical shape of approximately 40 km^2. This unit has a porphyritic texture with up to 42% modal abundance of K-feldspar megacrysts (2–5 cm long) in a medium-grained matrix composed of plagioclase, microcline, quartz and biotite. The first U-Pb zircon age for this unit is reported below (**Fig. 1b**).

Late aplitic to slightly porphyritic, centimeter to meters wide felsic dikes intruded all three units. Penecontemporaneous trachybasalt meters wide dikes mainly intrude the SBU and HU (Dahlquist et al., 2010; Alasino et al., 2012).

3. Methods

Below we present integrated field, structural, geochemical and U-Pb geochronological analyses of the SBIC. More information about analytical methods is included in the Electronic Supplementary Data.

3.1. Fieldwork in the northern part of the Sierra de Velasco

Field mapping in the northern part of the Sierra de Velasco was carried out from 2012 to 2015. It was completed after a great deal of fieldwork at a scale of 1:40,000, and it focused on identifying variations in composition, phenocryst abundance, enclave orientations, intrusive contacts and foliation types. About 750 measurements of orientation (strike and dip) of such features were taken throughout the mapped region. All data are included in the simplified geological maps of Figures 3 and 7.

3.2. Crystal size distribution analysis

To better understand the origin of the multiple magmatic fabrics in the SBIC, a crystal size distribution analysis was performed (e.g. Higgins, 1999; Higgins, 2006; Jerram and Higgins, 2007). This study was completed using digital length and width measurements using image analysis of all megacrysts captured in field photographs from seven selected localities.

3.3. Geochronological and geochemical data

Three samples were collected for U-Pb zircon dating and Hf-isotopes studies. These samples were analysed for whole-rock major oxides and trace elements in the GeoAnalytical Laboratory of the School of Earth and Environmental Sciences at Washington State University using a ThermoARL sequential X-ray fluorescence spectrometer, following the

procedure described by Johnson et al. (1999). Trace element compositions were determined using an Agilent 7700 ICP-MS, following the procedure described in the Electronic Supplementary Data. Whole-rock chemistry analyses are listed in Table 1.

U-Pb zircon dating by LA-ICP-MS was carried out at the Geochronological Research Center at Sao Paulo University in Brazil using a 193nm excimer laser coupled to a Neptune multicollector, double-focusing, magnetic sector ICP-MS. Operating procedures and parameters are discussed in Sato et al. (2011). The results are given in Table 2. LA-MC-ICP-MS Lu-Hf isotope analyses on zircon were conducted in the same research center using a Photon laser system (Sato et al., 2010) coupled to a Thermo-Finnigan Neptune MC-ICP-MS with 9 Faraday collectors. The results are given in Table 3.

Sr and Nd isotopic analyses of four whole rock samples (the three dated granitoids and a trachybasalt dike in the SBU) were carried out at the Geochronology and Isotope Geochemistry Center at Complutense University (Madrid, Spain) using an automated multicollector VG® SECTOR 54 mass spectrometer. The results are shown in Table 4. Additionally, Sr and Pb isotope analyses of two mineral zones from one K-feldspar megacryst were determined at the University of Arizona. The isotopic ratios of $^{87}Sr/^{86}Sr$ and the trace element concentrations of Rb and Sr of the mineral zones (see figure in the Electronic Supplementary Data) were measured on an automated VG Sector multicollector instrument fitted with adjustable Faraday collectors and a Daly photomultiplier. Lead isotopes were analyzed on a GV Instruments (Hudson, NH) MC-ICP-MS. The detailed procedures are described in the Electronic Supplementary Data. The results are given in Table 5.

4. Main intrusive contacts in the SBIC

4.1. Contacts between outer plutonic units and host rocks

The outer SBIC units (AU and SBU) mostly intrude mylonitic rocks (**Fig. 3**) of probably Ordovician age (Larrovere et al., 2016). These host rocks preserve a record of ductile deformation that resulted in a foliation with an average orientation of 350°/60°W. Along the 20 km long southeastern contact with the SBU, the foliation in the mylonitic rocks displays variable attitudes. In the southern part of the mapped area (point 1 in **Fig. 3**) this metamorphic foliation is roughly concordant to the contact for about 3 km, striking ~ W-E and WNW-ESE and dipping (~49°-76° toward S-SW) (**Fig. 4a**).

Locally near the outer contacts with the mylonite, the typical porphyritic texture of the SBU is absent and an undeformed fine-grained rock occurs, with occasional K-feldspar megacrysts, that can be interpreted as a ~50 m thick chilled margin (point 1 on map in Fig. 3). Sometimes, a 10-20-cm-thick zone of weak ductile deformation occurs within this chilled margin of the SBU (**Fig. 4b**). Locally, in the southeastern contact (point 2 on map in **Fig. 3**), the generally NNW-SSE/N-S-striking mylonitic foliation is preserved, but dips gently to the west (~10°). In other places, the contact is strongly discordant cutting across the metamorphic foliation at a high angle (points 3 and 4, **Fig. 3**). The mylonitic foliation in the host rock thus is unchanged near the highly irregular plutonic complex contact.

In the northeastern part of the mapped area (point 5, **Fig. 3**), the highly irregular AU is in contact with Ordovician host rocks in which the regional foliation remains unchanged as the plutonic complex is approached. Figure 5 shows that at 1025 m a.s.l. (cross section A), this contact becomes a flat-lying pluton floor dipping 30° SSW overlying the host rock (**Fig. 4c**). At higher altitudes (about 1300 m a.s.l.) the contact is sub-vertical, dipping 75° N (cross section B) or displays a flat-lying floor dipping 30° SSW (cross section C), which suggests a

stepped margin of a floor-wall transition (**Fig. 5a**). Stoped blocks of the mylonitic rocks occur within both units (AU and SBU), with rotated orientations of the mylonitic foliation (e.g., 130°−160°/80° NE) that vary over meters to hundred meters (**Fig. 3**).

4.2. Contact between the Asha and San Blas units

A wall-to-roof transition between AU and SBU was mapped in the northern part of the area (**Fig. 3**). Here, AU overlies the SBU (**Fig. 4d**). The contact is relatively straight, but at meter-scale it can be irregular. No solid-state deformation was observed at the margin of the SBU (**Fig. 4e**). In map view, this contact tends to become horizontal with increasing elevation: at low altitude, the contact dips about 60-70° S, whereas at about 1900 m a.s.l. the dip is horizontal (**Fig. 5b**). Locally, small garnet-bearing leucogranitic bodies are observed at the contact. Magmatic foliations of both units locally change into sub parallelism near the contact. Additionally, relatively straight and subparallel schlieren and schlieren troughs (i.e., Paterson, 2009; Pinotti et al., 2016) occur in the SBU close to the contact. Aplite and pegmatite dikes are common in the SBU, which in places cut across the contact extending only a few meters into the AU. The wall-to-roof transition between the SBU against host rocks (i.e., AU and mylonite) suggests a roughly cylindrical three-dimensional intrusion geometry for the SBU (**Fig. 5b**).

4.3. Contact between the San Blas and Hualco units

The HU intrudes the SBU. The intrusive contact where SBU overlies the HU varies from sharp to gradational over ≤ 15 m and locally preserves evidence of mingling (**Fig. 4f**). Contact-parallel schlieren occurs in both units. As discussed above, magmatic foliations of

both units (but mainly in HU) locally change into sub-parallelism with the contact. In some places the HU cuts across the dominant magmatic fabric in the SBU. The dip of the contact is are generally moderate (from 30° to 60°) but also fluctuate from flat to subvertical orientations, showing stepped contacts tens of meters in length. Some early contacts locally preserve evidence of local flow of magma resulting in K-feldspar megacryst accumulations and felsic enclaves. A pluton roof-wall transition between HU and SBU in these contacts shows an approximate mushroom geometry (**Fig. 5c**).

5. Inclusions

In addition to the presence of xenoliths of the host rock in the outer plutonic units, three different inclusion types occur in the SBIC. They can be distinguished based on their mineralogy, compositions and textures: (1) biotite-rich enclaves in the AU; (2) pieces of slightly older genetically related plutonic rock (cognate inclusions) in the SBU; and (3) felsic microgranular enclaves formed from the dismembering of aplitic dikes in a magma mush (HU).

Enclaves in the AU are microgranular, rich in biotite (about 30 modal %), mostly elliptical with major axes < 20 cm long. Inclusions in the SBU are porphyritic or aplitic in texture, generally felsic in composition, elliptical or rectangular in shape and up to one meter in length (**Fig. 6a**). Enclaves in the HU are microgranular, felsic in composition, rounded to elongate, mostly flattened with sub-horizontal orientation and usually with lobate margins (**Fig. 6b**). Their major axes range from 10 to 150 cm in length.

6. Compound fabrics

Compound fabrics, a combination of multiple magmatic mineral fabrics and enclaves are recognized in the SBIC. All described magmatic mineral fabrics are defined by the alignment of K-feldspar megacrysts and to a lesser degree biotite. These magmatic foliations represent one or more different statistical maxima of mineral orientations in each plutonic unit. The orientations of the mineral fabrics and enclaves are documented below and shown in table 6 and figure 7.

6.1. Asha Unit

In the AU, one magmatic fabric (type A_1) with a NNW-SSE strike and steep dips toward the E prevails (**Figs. 3, 6c, 7**). This fabric was mapped throughout the unit except near the contacts with the host rock and SBU where the fabric is mostly deflected and flattened (type A_2). Type A_2 forms an asymmetrical, kilometer size fold (**Figs. 3, 7**). Occasionally, a third fabric with ~E-W strike (type A_3) and steep dip is observed. A_3 typically overprints A_1. Enclaves in the AU are elliptical with their long axes parallel to the main magmatic fabric (**Fig. 7**).

6.2. San Blas Unit

In the SBU, magmatic fabrics form a roughly concentric, steeply dipping pattern, which is subparallel to the SBU margin. In map view, the concentric pattern (defined as type SB_2) is not centered in the SBU but occurs farther north in the unit (**Figs. 3, 7**). In the stereographic plots, this fabric is not well represented as it has not yet been fully mapped (**Fig. 7**). Three other magmatic fabrics have been recognized (**Figs. 3, 6d, 7**): (1) a NNW-striking fabric (type SB_1) that dips towards both the E and W (average 358°/85°); (2) a sub-vertical E-striking

fabric (type SB_3), which dips towards both the S and N (average 88°/83°S), and (3) a sub-horizontal fabric (type SB_4). Types SB_3 and SB_4 foliations share a single subhorizontal lineation. Commonly, the NNW-striking fabric (type 1) dominates in the north of the unit and overprints type SB_2.

The orientation of the long axes of the enclaves is varied but with a predominance parallel to north-south and east-west fabrics (**Fig. 7**). Magmatic fabrics are sometimes deflected around them.

6.3. Hualco Unit

The HU displays similar magmatic foliations to the SBU (**Figs. 3, 7**). In the margin, the magmatic fabric forms a roughly concentric, steeply inclined pattern (defined as type H_2). Additionally, we measured: (1) a N-striking fabric (type H_1) with an average strike and dip of 356°/85°W, (2) an E-striking fabric (type H_3) with an average strike and dip of 86 °N and (3) a flat-lying fabric (type H_4). Enclaves are flattened into 'pancake' shapes and have varied orientations, but with a predominance parallel to the northern fabrics (i.e., type H_1). A few enclaves exhibit quadruple pronged forms where both long and intermediate axes form elliptical ends parallel to magmatic fabrics in their immediate host (HU).

7. Whole-rock geochemistry

7.1. Major elements

Although the units of the SBIC are classified as A-type (e.g., Dahlquist et al., 2010), some distinctions between them are observed. These intrusive units are fairly evolved with SiO_2

content falling in a restricted range of 69.1 to 77.6 wt. % (n = 11, our three samples plus eight samples from Dahlquist et al., 2010; see Table 1 and Electronic Supplementary Data). On the alkalis vs. silica classification diagram of Wilson (1989), samples plot dominantly at the silica-rich end of the field of alkaline granitoids (**Fig. 8a**). They are moderately enriched in total alkalis (7.95–8.29 wt. %), with relatively high K_2O content ($K_2O/Na_2O \geq 1.42$). The granitic rocks are ferroan on the $FeO^t/(FeO^t+MgO)$ vs. SiO_2 diagram, but those of the AU fall at the border to the magnesian field (**Figs. 8b**). On the $Na_2O+K_2O–CaO$ vs. SiO_2 diagram, these samples follow a calc-alkalic to alkali-calcic trend (**Figs. 8c**).

Two samples of the AU are peraluminous (aluminum saturation index, ASI = 1.15–1.17), relatively rich in CaO (1.38–1.78 wt. %) and have high $FeO^t/(FeO^t+MgO)$ ratios (0.76–0.83). Rocks of the SBU are metaluminous to peraluminous (ASI = 0.98–1.13), poor in CaO (0.66–0.80 wt. %) and extremely rich in FeO^t relative to MgO with high $FeO^t/(FeO^t+MgO)$ ratios (0.87–0.98). Rocks of the HU (two samples) are metaluminous to peraluminous (ASI = 1.06–1.23), poor in CaO (0.80–1.15 wt. %) and rich in FeO^t relative to MgO with high $FeO^t/(FeO^t+MgO)$ ratios (0.87–0.89).

7.2. Trace elements

The granitic rocks of the AU and HU show a relative increase in REE fractionation ($[La/Yb]_N$ ranging from 6.6 to 10.2, n = 4) with respect to the granitic rocks of the SBU ($[La/Yb]_N$ ranging from 3.1 to 12.3, n = 7) (**Figs. 8d, e, f**). All granitic rocks show significant negative Eu anomalies although those of the SBU and HU are the most pronounced (AU, $[Eu/Eu]^*_N = 0.50$; SBU, $[Eu/Eu]^*_N = 0.07–0.31$; HU, $[Eu/Eu]^*_N = 0.19–0.31$) (**Figs. 8d, e, f**). Consistently, the Sr, Ba, and Eu content decrease from the AU (values ranging from Sr =

87−131 ppm, Ba = 402−452 ppm, Eu = 1.32−1.66 ppm) toward the SBU (values ranging from Sr = 17−49 ppm, Ba = 48−163 ppm, Eu = 0.45−0.81 ppm). The HU has intermediate values (values ranging from Sr = 37−63 ppm, Ba = 122−155 ppm, Eu = 0.59−0.90 ppm). High field strength elements such as Th, Y and Nb display the highest values in the SBU (values ranging from Th = 24−104 ppm, Y = 32−160 ppm, Nb = 23−136 ppm in the SBU to Th = 25−28 ppm, Y = 32−36 ppm, Nb = 19−22 ppm and Th = 34−50 ppm, Y = 46−49 ppm, Nb = 37−50 ppm in the AU and HU, respectively. Additionally, the high 10,000*Ga/Al ratio in the samples of the SBIC, a typical characteristic of the A-type granitoids (Whalen et al., 1987), commonly is higher in samples from the younger units (SBU = 2.8−4.8 and HU = 3.2) in comparison to those from AU (2.8−2.9) (Table 1 and Electronic Supplementary Data).

8. Geochronological and isotopic data

8.1. U-Pb LA-MC-ICP-MS zircon age and Hf in zircon isotope data

The combined SEM-CL and optical images reveal that the zircons separated from sample ASH-8 of the AU are mostly elongate prismatic grains with homogenous bright or oscillatory zoning (Table 2) and subhedral to euhedral-terminations (**Fig. 9a**). Analytical spots were mostly placed on the outer rims and the interior zones of the zircons. The majority of the analyses yielded zircon ages at about 340 and 452 Ma, respectively (details in Table 2). Five and seven data points yielded a Tera-Wasserburg Concordia age (Ludwig, 2003) of 340 ± 7 Ma and 452 ± 8 Ma, respectively (2 σ confidence limits, allowing for the uncertainty in U/Pb calibration). The first age is considered to be the best estimate for the crystallization of the host monzogranite. The second age is considered to be an inherited age (**Fig. 9a**). The Early Carboniferous zircons have variable εHf_t (t = 340 Ma) values ranging from −2.8 to −4.5

(Table 3). The average model age is calculated as 1.53 Ga (Table 3). The Ordovician zircons have variable εHf_t (t = 452 Ma) values ranging from −3.9 to −5.3. When the εHf_t is calculated for the Early Carboniferous time (t = 340 Ma), the values range from −6.3 to −7.6. The average model age is calculated as 1.66 Ga (Table 3).

The combined SEM-CL and optical images reveal that the zircons separated from sample SB-10 of the SBU are mostly elongate prismatic grains with oscillatory zoning or homogenous bright and subhedral to euhedral-terminations (**Fig. 9b**). Analysis spots were mostly placed on the outer, oscillatory zones of the grains (see Table 2). Seventeen data points yielded a Tera-Wasserburg Concordia age (Ludwig, 2003) of 344 ± 2 Ma (2σ confidence limits, allowing for the uncertainty in U/Pb calibration). This is considered the best estimate for the crystallization age of the monzogranite (**Fig. 9b**). No inherited ages were found. The zircons have variable εHf_t (t = 344 Ma) values ranging from +2.8 to −1.1 (Table 3), which are similar to those reported by Dahlquist et al. (2013) for the same unit (εHf_t from +1.6 to −6). The average model age is calculated as 1.13 Ga (Table 3).

The combined SEM-CL and optical microscope images revealed that the zircons separated from sample HUAL-9 of the HU are mostly elongate prismatic grains with oscillatory zoning or homogenous bright and subhedral to euhedral-terminations (Table 2 and **Fig. 9c**). Analytical spots were mostly placed on the outer oscillatory rims of the grains (see Table 2). Eleven data points yielded a Tera-Wasserburg Concordia age (Ludwig, 2003) of 346 ± 6 Ma (2σ confidence limits, allowing for the uncertainty in U/Pb calibration). This is considered the best estimate for the crystallization age of the HU monzogranite (**Fig. 9c**). No inherited ages were found. The Early Carboniferous zircons have variable εHf_t (t = 346 Ma) values ranging from +3 to −0.5 (Table 3). The average model age is calculated at 1.19 Ga (Table 3).

8.2. Rb-Sr and Sm-Nd whole rock isotope compositions

A reference age of 340 Ma, based on the U-Pb SHRIMP zircon age of a granite from the San Blas unit (sample VEL-6017, Dahlquist *et al.*, 2006) was used for calculating the isotope compositions of the samples. Average ages from the different igneous units referred to above produce a similar value of 343 Ma. The three dated samples from SBIC yielded $^{87}Sr/^{86}Sr_t$ and εNd_t values of 0.72440 and −5.9 for AU, 0.76431 and −1.1 for SBU and 0.77694 and −3.5 for HU, respectively (Table 4). The mafic dike of the USB yielded $^{87}Sr/^{86}Sr_t = 0.70489$ and $\varepsilon Nd_t = +2.2$ (Table 4). Additionally, four samples previously published in Dahlquist et al. (2010) yielded εNd_t values from +0.6 to –4.8 for the SBU (three samples) and a value of −1.5 for the HU (see Electronic Supplementary Data).

The calculated depleted mantle model ages (TDM; Table 4) vary from 1.01 Ga to 1.55 Ga, indicating that the crustal source contributing the Nd was Mesoproterozoic or older in age. Remarkably, the Hf-T_{DM} overlaps the Nd-T_{DM} values.

8.3. Rb-Sr and U-Pb isotope compositions of K-feldspar zones

Sr and Pb isotope analyses were conducted on the core and the rim of one K-feldspar megacryst collected in the SBU (Table 5 and Electronic Supplementary Data). The $^{87}Sr/^{86}Sr_t$ values of the K-feldspar yielded 0.72242 for the core and 0.71989 for the rim. The Pb isotope ratios yielded the following results for core and rim, respectively: $^{206}Pb/^{204}Pb$ = 18.80 and 18.40, $^{207}Pb/^{204}Pb$ =15.98 and 15.66 and $^{208}Pb/^{204}Pb$ = 39.11 and 38.30.

9. Discussion

9.1. A-type granite genesis

The crystallisation ages obtained from the Asha (ASH-8 = 340 ± 7 Ma), San Blas (SB-10 = 344 ± 2 Ma) and Hualco (HUAL-9 = 346 ± 6 Ma) units document that their emplacement was within the quoted errors and thus close in time. Nd whole rock and Hf zircon isotopes, however, reveal contrasting sources for these igneous units. ASH-8 has abundant inherited zircons (consistent with the peraluminous composition and an εNd_t value of −5.9) and all εHf_t values are negative (from −2.8 to −7.6, Table 3). When the εHf_t for Ordovician inherited zircons is calculated for Early Carboniferous time, the εHf_t have similar values to those of Early Carboniferous zircons (t = 340 Ma, Table 3), consistent with a dominant continental crust source of Ordovician age. SB-10 zircons (Table 3), together with those reported by Dahlquist et al. (2013) for the same unit, define positive and negative εHf_t values (from +2.6 to −6, n=19), which is consistent with interaction between continental crust and juvenile magmas. The wide range of εNd_t values of the granitic samples of the SBU (from +0.6 to −4.8) further suggests that such interaction was not fully homogenized. The most differentiated granitic rocks in the SBU (such as SBP-10, $SiO_2 \sim 76$ wt. % and $\varepsilon Nd_t = +0.6$) have similar εNd_t values to that of the analyzed sample of a mid-alkaline mafic dike ($\varepsilon Nd_t = +2.2$, Table 4), which suggests that the most differentiated granitoids could be genetically related to the mafic component. Some Hf analyses from HUAL-9 failed because the laser burnt through the grain completely before sufficient data had been obtained. Three acceptable analyses yielded positive and negative εHf_t values for the HU (from +3. to −0.5, Table 3), with a similar range to that reported for SB-10. The most straightforward conclusion is that, unlike the AU magmas that have a dominant crustal source component, the younger units (SBU and HU) can be reconciled with open-system, mantle-crust interactions. This is compatible with the

evolution shown by the A-type magmatism in the region, where the older magmas resulted from reworking of supracrustal material whereas and the youngest magmas resulted in part from reworking of supracrustal material but with a variable contribution of juvenile magmas (**Fig. 10**) (e.g., Rapela et al., 2008; Dahlquist et al., 2010, 2013, Alasino et al., 2012).

Two end-member A-type granitoids are recognized. The first group includes the peraluminous granitic rocks of the AU that have abundant inherited Ordovician zircons and negative εHf_i and εNd_i isotope values. This group has lower SiO_2 (~ 69 wt. %), but is slightly enriched in MgO (0.6−0.9 wt. %), CaO (1.4−1.8 wt. %), Sr (87−116 ppm) and Ba (402−445 ppm). The second group comprises the metaluminous granitic rocks of the SBU (e.g., SB-10), with positive and negative values of εHf_t and εNd_t values close to zero. They have higher SiO_2 (74−78 wt. %) but lower MgO (≤ 0.2 wt. %), CaO (≤ 0.8 wt. %) and Sr (SBU 16−45 ppm). This group has higher Ga/Al ratios, as well as a more pronounced Eu anomaly than the crustal-derived melts of the first group, suggesting that the metaluminous granitic rocks can be residual products of the fractionation of mafic magmas under low pressure conditions (≤ 5 kbar) with some crustal assimilation (e.g., Frost and Frost, 2011).

The increase of negative Eu anomalies together with the concomitant increase of Sr, Ba, and Eu in both SBU and HU compared to the AU suggests feldspar segregation during the crystallization process. Significant feldspar fractionation would occur during the crystallization of SBU and HU while it was less important in the AU. The higher HFSE (e.g., Th, Y, Nb, Ta) values in the SBU suggest a greater role of crystallization and accumulation of accessory minerals (e.g., monazite) in this granitic unit.

9.2. Deflection and removal of the host rock

At shallower crustal levels, such as the northern margin of the AU, the metamorphic host rock shows brittle behavior during emplacement. Contacts are sharp and irregular and sometimes exhibit a chilled margin that suggests that they are early preserved contacts. These early contacts display no emplacement-related ductile deformation. In other places, stoped blocks of the host rock with rotated fabrics in AU, suggest that magmatic stoping was involved in the growth of the intrusive complex. Furthermore, the metamorphic foliation of the host rock maintains a regional pattern (~ NNW-SSE strike) to the north of the pluton contact documenting an absence of extensive faulting or detachment of the roof (**Fig. 3**). At least in this area, this dismisses a lateral dilatational opening of the wall-rock as the mechanism for creating space. Here, the contact orientation changes abruptly without corresponding changes in the attitude of the mylonitic foliation in the host rock, implying vertical rather than horizontal material transfer (e.g., Paterson and Vernon, 1995). This is consistent with the inferred stepped geometry of the AU floor-wall transition (**Fig. 5a**), where the main room making mechanism could be either piecemeal floor subsidence or formation and sinking of multiple host-rock blocks (e.g., Yoshinobu et al. 2003; Tomek et al., 2014).

The intrusive contact at the southern margin (i.e., SBU against mylonitic host rocks) documents that the host rock locally behaved ductilely during emplacement (**Figs. 3, 6a**). The regional metamorphic foliation (NNW-SSE) is deflected (~E-W) into parallelism with the contact and dips about 60° S at 1250 masl, in a zone about 500 m thick. Additionally, the weak solid-state deformation in the chilled granite margins suggests that these also were early contacts; i.e., they not were destroyed by late processes in the construction of the complex. Therefore, based on deflections of host rock markers in the wall (e.g., mylonitic foliation), we calculate a shortening of 42 %, which indicates that an expansion of the host granitoid of about 400 m, representing 7 % of radius of the SBU, helped create space. In other domains in

the aureole, the regional metamorphic foliation of the host rock is commonly cut off by an abrupt irregular intrusive contact, which together with the presence of mylonitic xenoliths in the SBU, imply that magmatic stoping removed parts of the early contacts. This removal is evident around the SW part of the pluton (**Fig. 3**). This segment, possibly weakened by the preexisting direction of the metamorphic foliation (almost parallel to the contact) appears highly irregular.

Consistent with the host foliation deflection along the southern margin, type A_1 magmatic foliation in the AU is strongly deflected generating a margin parallel foliation around SBU (**Figs. 3, 7**). Type A_2 forms an asymmetrical fold of kilometers in size. The amount of calculated shortening, up to 30 %, indicates that a maximum expansion of the host granitoid of 690 m (a 12 % of radius of the SBU) occurred by the expansion of the SBU intrusion. Finally, the main body of the HU, which shows a mingling relationship with the SBU host rock, and has an approximate mushroom geometry defined by the early contacts, suggest that this body could have intruded into already emplaced magma mush (SBU) making space by the displacement of the SBU magma mush. An interpretive block-diagram illustrating the emplacement mechanisms in the SBIC is shown in Figure 11.

9.3. Interpretation of the compound fabrics in the SBIC

9.3.1. Magmatic fabrics

At least four distinct magmatic fabrics are preserved in the SBIC: type 1 (~N-S), type 3 (~E-W) and type 4 (flat) occur in all units; margin parallel type A_2 is in AU, and types SB_2 and H_2 occur in SBU and HU, respectively (Table 6). Figure 7 shows important changes in orientation and intensity of the main fabrics in each unit, indicating that fabrics record

different strain increments through time. Type A_1 occurs across the entirety of AU but near the contacts with SBU this fabric is deflected and flattened to a new orientation, which is why it is here classified as type A_2. We interpret that the latter fabric is formed by strain of the crystal mush during the upward flow of the magma that is moving along the rigid boundaries of the SBU during its emplacement. On the other hand, in SBU and HU the ~N-S type 1 fabric commonly overprints the concentric type 2 (SB_2 and H_2), indicating that type 1 fabric is the oldest in the AU but is younger in the SBU and HU. Additionally, types SB_2 and H_2 are modifications to the ~E-W type-3 fabric (or vice versa).

Previous explanations for the formation of multiple fabrics in a single pluton or igneous unit (e.g., Žák et al., 2007) include: (1) differential rotation of minerals with different shapes or axial ratios during noncoaxial strain (Blumenfeld and Bouchez, 1988), (2) formation of orthogonal lineations where minerals with different axial ratios are aligned parallel to unequal elongation components during coaxial flow (Ježek et al., 1994; Schulmann et al., 1997), (3) formation of metastable orthogonal lineations under a combination of pure and simple shear (Willis, 1977), and (4) formation of fabrics, which record different strain increments thus recording the temporal evolution of strain in a magma chamber (Paterson et al., 2003; Žák et al., 2007). In order to evaluate a mechanical effect for the origin of such fabrics (e.g., type 3 overprinting type 1 in AU and type 1 overprinting types 2 and/or 3 in SBU and HU) caused by relative differences in crystal size (causes 1 and 2 listed above), a crystal size distribution (CSD) analysis was performed (e.g. Higgins, 1999; Higgins, 2006; Jerram and Higgins, 2007). The data indicate that crystals of about 19–28 mm length are most common, and are equally represented in the two crystals populations belonging to the two respective main foliation planes (**Figs. 12a-g**). This indicates that causes (1) and (2) are not applicable to the SBIC. When both populations (i.e., types 1 and 3 for AU, and types 1 and 2-3 for SBU and

HU) are analyzed together, the population density curve in the CSD analysis show a characteristic shape, with an exponential decrease in the number of larger crystals, from 22 to 75 mm, and an exponential drop below 19 mm (**Fig. 12h**). In cases where differences were found, the dominant population (or dominant fabric) in SBU showed a tendency to be associated with larger crystal sizes suggesting that these crystals had a harder time rotating (from E-W to N-S) in the magma mush during a shift in the strain field.

9.3.2. Inclusions

Enclaves in all plutonic units provide evidences that enclaves experienced complex magmatic histories involving early magmatic strain, subsequent rigid rotations, and potentially late increments of strain. The long axes of the enclaves and cognate inclusions in AU and SBU are parallel to the main magmatic fabrics while the felsic enclaves in the HU have different orientations but with a preferential ~N-S orientation (i.e., type-1). This difference is because the former were rigid objects, while those in the HU were mingled during the dismemberment of aplitic dikes into the magma mush. This allowed the enclaves of the HU to register an intracrystalline magmatic deformation (e.g., Vernon et al., 1988). They are flattened in concordance with the type-4 fabric in the HU, but their long axes shows different orientations because most of them are unable to rotate as rigid objects in a crystal-rich mush. Figure 6b shows two perpendicularly oriented enclaves in HU, the small inclusion is oriented ~N-S but the larger one is oriented ~E-W with prongs parallel to long axis of the first enclave. This indicates that small enclaves (about 10 cm or less) maintain the ability to rotate and orient parallel to the last strain increment (i.e., ~N-S type-1), whereas the remaining inclusions instead develop prongs parallel to the type-1 mineral fabric.

9.3.3. Chronology and possible origins of the compound fabrics

The formation of the multiple magmatic fabrics and their relationship with enclaves in the SBIC provide an interesting example of the temporal history of the strain fields in a magma chamber that formed by successive batches of magma (**Figs. 3, 7**) (Table 6). As already noted, the crystallization ages of the plutonic units overlap within analytical error (*see section 3*). However, the relationship of intrusive contacts between these units argues that fabric acquisition in the SBIC was likely restricted in time, with the fabrics of the outer unit (AU) formed in a highly-crystalline magma mush (still above its solidus) while the formation of fabrics in the inner units (SBU and HU) overlap in age.

Field relationships indicate that the type 1 fabric (and enclaves parallel to it) in AU (A_1 fabric) is the oldest in the SBIC. This fabric with a NNW-SSE strike is widely prevalent in contemporaneous plutons, such as the Huaco (357 ± 3 Ma) and La Chinchilla (345 ± 1 Ma) plutons in the central part of the Sierra de Velasco (Macchioli Grande et al., 2015). This suggests that type 1 could be linked to regional strain field with WSW-ENE shortening and NNW-SSE stretching directions. Once it was formed, the upward pushing of SBU against the AU formed type A_2 fabric, which recorded strain increments caused by boundary flow along margins of the igneous complex.

The concentric fabrics in SBU and HU together with flattened type 4 (also measured in the felsic enclaves), indicate that these composite fabrics formed by superposition of two different strain increments (e.g., Paterson et al., 2003; Žák et al., 2007; Pinotti et al., 2016). The regional strain field represented by the type-1 fabric was overprinted temporarily during the formation of the concentric fabric pattern plus the flattened type (type 4). The latter is

product of deformation of early magma batches by later magma pulses (Schmeling et al., 1988; Cruden, 1990; Paterson and Vernon, 1995) in vicinity of the roof of the chamber.

Finally, the formation of the ~ E-W type-3 fabric in the SBIC is problematic. Type 3 fabric appears subordinate in AU as the last formed increment of deformation but is usual in SBU and HU where commonly the ~ N-S type-1 fabric overprinted it. Type-3 fabric might thus be diachronous and reflect local processes rather than regional strains.

9.4. Insight into magma plumbing systems

The SBIC grew during three periods of magma additions that are characterized by variations in the magma sources and the emplacement style through time. A compilation of all zircon ages in Figure 13 suggests that it may have taken several millions of years (about 6 Ma between the older and younger ages) for the construction of the SBIC. However, this period of time is unreliable if it is obscured by mixed zircon populations, including xenocrysts (inherited from older host rocks or melt source regions), antecrysts (recycled from earlier magmas) and autocrysts (grown in the final melts) (e.g., Hildreth, 2004; Bacon and Lowenstern, 2005; Miller et al., 2007; Memeti et al., 2014). We speculate that the age distribution of the magmatism is biased toward the youngest phases of plutonism; most of the grains that yield older ages are in the youngest igneous units (e.g., HU) (**Fig. 13**). Therefore, the period of time for the construction of the SBIC should be more restricted and within the error range, probably no more than 2-3 million years, which is consistent with multiple magma batches showing deflection of magmatic fabric in the host granitoid, mingling relationships and gradational contacts (see previous sections).

Evidence of magma mixing is usually well preserved in volcanic rocks, but may be obscured in plutonic systems as a result of chemical re-equilibrium between the end-member magmas at temperature above the solidus (e.g., Anderson, 1976; Kemp et al. 2007). In SBIC, the Hf isotopic diversity within magmatic zircons in the younger units and the spectrum of Nd isotope ratios of the bulk magma samples of the SBU suggest that at least the SBU chamber was made up of smaller batches. In our model (see next), the silica-rich juvenile magmas injected into a lower crustal magma reservoir, generated multiple and rising viscoplastic heterogeneous magma batches (e.g., Bergantz et al., 2015). If this is correct, the spectrum both in crystallization ages and values of εHf_i in zircons from younger units were formed not only by mixing of zircon populations during ascent and/or recycling of earlier magmas at the emplacement site, but also by disparate chemical conditions in the crystal-melt interface from a heterogeneous mixture (e.g., Bergantz et. al., 2015) which formed zircon crystals of similar crystallization ages but with different isotopic signatures. This model, which requires a short residence time of magma batches in the lower crust, may be reconciled with the proposed retro-arc setting (e.g., Alasino et al., 2012), where magmas are quickly extracted to ascend to shallow levels in order to balance the high thermal difference between lower and upper parts of a thinned crust.

9.5. Evolution of magma bodies into upper crust

Our model for the evolution of the SBIC includes the accommodation of at least three major batches of magma assembled incrementally in the upper crust (**Fig. 14**). Unlike episodes of short duration of thousands of years (e.g., Michel et al., 2008), the thermal maxima in the SBIC increased over time (≤ 2-3 m.y.) resulting in a shift in the style of

emplacement and composition of the magmas (e.g., Yoshinobu et al., 1998). At first, magma derived from dominantly Ordovician crustal sources ascended under a regional strain field dominated by ~WSW-ENE shortening, to form the AU (**Fig. 14a**). This resulted in a tabular to funnel-shaped intrusion likely fed by one or more subvertical conduits (**Fig. 14b**), surrounded by host rock deforming by brittle processes (e.g., Cruden et al., 1999; Brown and McClelland, 2000; Annen 2011). Subsequently, the SBU magmas were able to ascend in a pre-heated pathway allowing it to gradually change into batches with vertically elongated visco-elastic diapirs (e.g., Paterson and Vernon, 1995; Miller and Paterson, 1999, del Potro et al., 2013; Best et al., 2016) (**Fig. 14c**). Here, both brittle and ductile host rock deformation is consistent with the observed stoped blocks, and downward transport together with contraction of wall rock. The lack of large deflections in the wall-host rock requires the operation of vertical material transfer mechanisms, such as floor-subsidence of the AU chamber and recycling the older batches of the SBU (e.g., Miller and Paterson, 2001; Gasching et al., 2016; Paterson et al., 2016) (**Fig. 14b**). Finally, HU magmas that entered immediately after the formation of SBU magma mush could have intruded as visco-plastic diapirs (**Fig. 14c**).

We envisage that the input of juvenile mafic magma into the crust probably by lithospheric removal in the continental back-arc (e.g., Alasino et al., 2012), created a widespread heating at mid-to-lower crustal levels (<35 to 40 km) and generation of silica-rich magmas by extreme differentiation of basaltic melts. This allowed pulses of magma to gradually move upwards by taking advantage of pre-heated channel pathways that formed the AU (e.g., Cao et al., 2016). The existence of more than one population of early igneous mineral phases (such as zircon) in the younger units (SBU and HU), together with other mineral phases (such as K-feldspar) nucleated in the SBU displaying from core to rim more primitive isotope

composition patterns, suggest that the younger units were formed by a heterogeneous mixture between the juvenile silicic magmas and crustal components (e.g., Bergantz et al., 2015).

The length of time required to store heat in the crust and produce a thermally mature system is uncertain. However, a rough estimation of up to 2-3 m.y is possible in our model. This is compatible with a model where a partially molten lower crustal zone first resulted in segregation of crustal-derived magmas, followed by injection of juvenile magmas producing a heterogeneous mixture of magmas ascending together, probably driven by buoyancy with simultaneous host rock downward flow (e.g., Saleeby et al., 1990; Paterson and Farris, 2008).

9.6. Implications for volcanic systems

The compositional variation in eruptions from a single volcanic center is often attributable to crystal-liquid fractionation and/or syn-eruptive mixing (e.g., Cioni et al., 1995; Tornare et al., 2016). However, volcanoes containing multiple crystal rims without sharing the isotopic composition of the groundmass or with an increase in the primitive character of their products over time, argue that the origin of the volcanism can be more complex (e.g. Hildreth, 2004; Eichelberger et al., 2006; Davidson et al., 2007). To shed light on this issue, our results support that several chambers may grow at shallow crustal levels in a single plumbing system, allowing complex interactions between liquid-liquid and liquid-solid materials that are not in isotopic equilibrium. This implies that pre-mixing of magmas could occur before eruption, and zoning of crystals would reflect complex processes in magma plumbing and not during eruption as is sometimes inferred. Moreover, the rapid ascent of magmas that feed eruptions in a mature system could occur within a hot magma mush, which allows the generation the multiple ephemeral chambers with a ductile downward flow of the host rock.

10. Conclusions

An integrated field, structural, geochemical, isotopical and U-Pb geochronological study of the northwestern Sierra de Velasco, NW Argentina, indicates that the SBIC represents a dynamic plutonic complex resulting in the formation of at least 3 separate chambers at upper crustal levels. Three main igneous units with crystallization ages close in time and within the error range are recognized. Intrusive units and contact relationships, from older to younger, are:

(1) Asha unit (340 ± 7 Ma): a tabular to funnel-shaped intrusion, discordant contacts with the regional host-rock structures, composed of peraluminous two-mica granitoids. The dated sample yielded a value of $\varepsilon Nd_t = -5.9$ and its Carboniferous magmatic zircons have variable εHf_t values ranging from −2.8 to −4.5. The average zircon Hf model age is calculated as 1.59 Ga.

(2) San Blas unit (344 ± 2 Ma): consists of an approximately cylindrical-shaped intrusion built by multiple smaller magma batches, of metaluminous to weakly peraluminous composition. This unit presents abundant stoped blocks (many of them are of cognate origin) and their intrusive contacts document some displacement of the host rock by ductile flow of about 35 % shortening. The granitic rocks, with biotite dominant, yielded εNd_t values from +0.6 to –4.8. The dated samples have two contrasting isotopic compositions, defining positive and negative εHf_t values (+2.6 to −6). The average zircon Hf model age is calculated as 1.25 Ga

(3) Hualco unit (346 ± 6 Ma): consists of peraluminous granitic rocks, with dominant biotite, with a possible mushroom geometry and concordant to regional host-rock structures.

Two granitic rocks yielded εNd_t values of –1.5 and –3.5. The Early Carboniferous zircons have εHf_t values ranging from +3 to –0.5. The average model age is calculated as 1.19 Ga

The evolution of the SBIC includes the amalgamation of multiple batches of magmas assembled incrementally into upper crust. We visualize a scenario whereby crustal-derived magmas are followed by juvenile silicic magmas, which mix with partial molten crustal materials, and gradually move upwards by taking advantage of pre-heated channel pathways of the previous intrusions. As the plutonic system matures, the ascent of magmas is governed by the visco-elastic flow of host rock, or if the magma batches rise within a hot magma mush (such as HU in SBU) its ascent could result in ductile downward flow of the host rock.

The formation of A-type granites in the SBIC involved crustal-derived magmas at beginning, but with a variable mixing of these with juvenile magmas at the end. Geochemically, juvenile magmas are characterized by a higher content in silica and Ga/Al ratio, as well as a more pronounced Eu anomaly than the crustal-derived melts, suggesting that the former can be residual products of the fractionation of mafic magmas under low pressure conditions ($\leq$ 5 kbar). In this model, the initial partial melting in the crust could reflect underplating/intraplating of mafic magmas at the base of the crust in a retro-arc setting.

One general conclusion of this study is that the thermal maturity of an upper crustal section can be achieved by episodic intrusions through time (thousands to millions years). This can lead to (1) ascent of multiple magma batches (mostly non-consanguineous) in the same pre-heated pathway, together with a downward transfer of materials towards magma source regions; (2) complex interactions between liquid-liquid and liquid-solid materials not in isotopic equilibrium; (3) changes in the shape of plutonic bodies, which range from tabular to vertically elongated bodies; and (4) formation of multiple magmatic fabrics recording the

changes in the strain field over time. Unlike concepts in which magmas are mixed, contaminated and homogenized at the lower crust (e.g., a MASH zone), our data suggest that magma diversification processes can be highly dynamic and occur along a single plumbing system when the upper crust is thermally mature. If this plumbing system feeds eruptions, the re-use of the same pathway by distinct magmas will allow the generation of multiple ephemeral reservoirs.

Acknowledgements

This work was supported by Argentine public grants FONCYT PICT 2013-0226 and SECyT-UNLaR 0599/2011. We thank numerous UNLaR undergraduate students for their assistance during fieldwork. P.H. Alasino thanks Carlos Bustamante and Sergio de La Vega for technical support. V. Memeti acknowledges a Jr/Sr grant from Cal State Fullerton that funded the K-feldspar analyses and Dr. Mihai Ducea at the University of Arizona for providing the lab space to conduct the study. We thank L. Pinotti (UNRC) and an anonymous reviewer for useful reviews and N. Eby (editor-in-chief) for his valuable editorial assistance. Rohini Shivaram (ELSEVIER journal manager) is thanked for her timely help with communications and production.

References

Alasino, P. H., Dahlquist, J. A., Galindo, C., Casquet, C., Saavedra, J., 2010. Andalusite and Na- and Li-rich cordierite in the La Costa pluton, Sierras Pampeanas, Argentina: textural and chemical evidence for a magmatic origin. International Journal of Earth Sciences 99, 1051–1065.

Alasino, P. H., Dahlquist, J. A., Pankhurst, R. J., Galindo, C., Casquet, C., Rapela, C. W., Larrovere, M., Fanning, C. M., 2012. Early Carboniferous sub- to mid-alkaline magmatism in the Eastern Sierras Pampeanas, NW Argentina: a record of crustal growth by the incorporation of mantle derived material in an extensional setting. Gondwana Research 22, 992–1008.

Anderson, A. T., 1976. Magma mixing: petrological process and volcanological tool. Journal of Volcanology and Geothermal Research 1, 3–33.

Annen, C., 2011. Implications of incremental emplacement of magma bodies for magma differentiation, thermal aureole dimensions and plutonism-volcanism relationships. Tectonophysics 500, 3–10.

Bachmann, O., Bergantz, G. W., 2004. On the origin of crystal-poor rhyolites: extracted from batholithic crystal mushes. Journal of Petrology 45, 1565–1582

Bacon, C. R., Lowenstern, J. B., 2005. Late Pleistocene granodiorite source for recycled zircon and phenocrysts in rhyodacite lava at Crater Lake, Oregon. Earth and Planetary Science Letters 233, 277–293.

Báez, M. A., Basei, M. A., Toselli, A. J., Rossi, J. N., 2004. Geocronología de granitos de la sierra de Velasco (Argentina): reinterpretación de la secuencia magmática. Actas Simposio 40 años de geocronología en Brasil, San Pablo, Brasil, p. 85.

Bergantz, G. W., Schleicher, J. M., Burgisser, A., 2015. Open-system dynamics and mixing in magma mushes. Nature geoscience 8, 793–796.

Best, M. G., Christiansen, E. H., de Silva, S., Lipman, P. W., 2016. Slab-rollback ignimbrite flareups in the southern Great Basin and other Cenozoic American arcs: A distinct style of arc volcanism. Geosphere 12, 1–39.

Blichert-Toft, J., Albarède, F., 1997. The Lu-Hf isotope geochemistry of chondrites and the evolution of the mantle-crust system. Earth Planetary Science Letters 148, 243–258. Erratum: Earth Planetary Science Letters 154 (1998), 349.

Brown, E. H., McClelland, W. C., 2000. Pluton emplacement by sheeting and vertical ballooning in part of the Southeast Coast plutonic complex, British Columbia. Geological Society of America Bulletin 112, 708–719.

Blumenfeld, P., Bouchez, J. L., 1988. Shear criteria in granite and migmatite deformed in the magmatic and solid states. Journal of Structural Geology 10, 361–372.

Cao, W., Kaus, B. J. P., Paterson, S., 2016. Intrusion of granitic magma into the continental crust facilitated by magma pulsing and dike-diapir interactions: Numerical simulations. Tectonics 35, 1575–1594.

Cawood, P. A., 2005. Terra Australis Orogen: Rodinia breakup and development of the Pacific and Iapetus margins of Gondwana during the Neoproterozoic and Paleozoic. Earth-Science Reviews 69, 249–279.

Cioni, R., Civetta, L., Marianelli, P., Metrich, N., Santacroce, R., Sbrana, A., 1995. Compositional layering and syn-eruptive mixing of a periodically refilled shallow magma chamber: the AD 79 Plinian eruption of Vesuvius. Journal of Petrology 36, 739–776.

Coira, B., Cisterna, C. E., Ulbrich, H. H., Cordani, U. G., 2016. Extensional Carboniferous magmatism at the western margin of Gondwana: Las Lozas valley, Catamarca, Argentina. Andean Geology 4, 105–126.

Cruden, A. R., 1990. Flow and fabric development during diapiric rise of magma. Journal of Geology 98, 681–698.

Cruden, A. R., Tobisch, O. T., Launeau, P., 1999. Magnetic fabric evidence for conduit-fed emplacement of a tabular intrusion: Dinkey Creek Pluton, central Sierra Nevada batholith, California. Journal of Geophysical Research 104, 511–530.

Dahlquist, J. A., Pankhurst, R. J., Rapela, C. W., Casquet, C., Fanning, C. M., Alasino, P., Baez, M., 2006. The San Blas Pluton: an example of Carboniferous plutonism in the Sierras Pampeanas, Argentina. Journal of South American Earth Sciences 20, 341–350.

Dahlquist, J. A., Alasino, P. H., Eby, G. N., Galindo, C., Casquet, C., 2010. Fault controlled Carboniferous A-type magmatism in the proto-Andean foreland (Sierras Pampeanas, Argentina): geochemical constraints and petrogenesis. Lithos 115, 65–81.

Dahlquist, J. A., Pankhurst, R. J., Gaschnig, R. M., Rapela, C. W., Casquet, C., Alasino, P. H., Galindo, C., Baldo, E. G., 2013. Hf and Nd isotopes in Early Ordovician to Early Carboniferous granites as monitors of crustal growth in the Proto-Andean margin of Gondwana. Gondwana Research 23, 1617–1630.

Davidson, J. P., Morgan, D. J., Charlier, B. L. A., Harlou, R., Hora, J. M., 2007. Microsampling and Isotopic Analysis of Igneous Rocks: Implications for the Study of Magmatic Systems. Annual Review of Earth and Planetary Sciences 35, 273–311.

De Paolo, D. J., Linn, A. M., Schubert, G., 1991. The continental crustal age distribution: methods of determining mantle separation ages from Sm–Nd isotopic data and application to the Southwestern United States. Journal of Geophysical Research 96, 2071–2088.

de Silva, S. L., Gosnold, W. D., 2007. Episodic construction of batholiths: Insights from the spatiotemporal development of an ignimbrite flare-up. Journal of Volcanology and Geothermal Research 167, 320–335.

de Silva, S., Zandt, G., Trumbull, R., Viramonte, J. G., Salas G., Jiménez, N., 2006. Large ignimbrite eruptions and volcano-tectonic depressions in the Central Andes: a thermomechanical perspective. In: Troise, C., De Natale, G., Kilburn, C. R. J. (Eds.), Mechanisms of Activity and Unrest at Large Calderas. Geological Society, London, Special Publications, 269, 47-63.47–63.

del Potro, R., Díez, M., Blundy, J., Camacho, A. G., Gottsman, J., 2013. Diapiric ascent of silicic magma beneath the Bolivian Altiplano. Geophysical Research Letters 40, 2044–2048.

Farina, F., Dini, A., Innocenti, F., Rocchi S., Westerman, D. S., 2010. Rapid incremental assembly of the Monte Capanne pluton (Elba Island, Tuscany) by downward stacking of magma sheets. Geological Society of America Bulletin 122, 1463-1479.

Frost, C. D., Frost, B. R., 2011. On ferroan (A-type) granitoids: their compositional variability and modes of origin. Journal of Petrology 52, 39 53.

Frost B. R., Barnes C. G., Collins W. J., Arculus R. J., Ellis, D. J., Frost C. D., 2001. A geochemical classification for granitic rocks. Journal of Petrology 42, 2033–2048.

Gaschnig, R. M., Vervoort, J. D., Tikoff, B., Lewis, R. S., 2016. Construction and preservation of batholiths in the northern U.S. Cordillera. Lithosphere L497.1.

Gregori, D.A., Fernández-Turiel, J.A., López-Soler, A., Petford, N., 1996. Geochemistry of Upper Paleozoic-Lower Triassic granitoids of the Central Frontal Cordillera (33°10'-33°45'), Argentina. Journal of South American Earth Sciences 9, 141-151.

Grosse, P., Söllner, F., Baéz, M. A., Toselli, A.J., Rossi, J. N., de la Rosa, J. D., 2009. Lower Carboniferous post-orogenic granites in central-eastern Sierra de Velasco, Sierras Pampeanas, Argentina: U–Pb monazite geochronology and Sr–Nd isotopes. International Journal of Earth Sciences 98, 1001–1025.

Higgins, M. D. 1999. Origin of megacrysts in granitoids by textural coarsening. In: Castro, A., Fernandez, C., Vigneresse, J. L. (Eds.), Understanding granites: integrating modern and classical techniques: Geological Society, London, Special Publications 168, 207–219.

Higgins, M. D., 2006. CSD Corrections (Computer Software). 1.3.7.1, August 2006.

Hildreth, W., 2004. Volcanological perspectives on Long Valley, Mammoth Mountain, and Mono Craters: several contiguous but discrete systems. Journal of volcanology and Geothermal Research 136, 169–198.

Ježek, J., Melka, R., Schulmann, K., Venera, Z., 1994. The behaviour of rigid triaxial ellipsoidal particles in viscous flows—modeling of fabric evolution in a multiparticle system. Tectonophysics 229, 165–180.

Jordan, T., Allmendinger, R., 1986. The Sierras Pampeanas of Argentina: a modern analogue of Rocky mountain foreland deformation. American Journal of Science 286, 737–764.

Jordan, T. E., Zeitler, P., Ramos, V. A., Gleadow, A. J. W., 1989. Thermochronometric data on the development of the basement peneplain in the Sierras Pampeanas, Argentina. Journal of South American Earth Sciences 2, 207–222.

Jerram, D. A., Higgins, M. D., 2007. 3D analysis of rock textures: Quantifying igneous microstructures. Elements 3, 239–245.

Johnson, D. M., Hooper, P. R. & Conrey, R. M. (1999). XRF analysis of rocks and minerals for major and trace elements on a single low dilution Li-tetraborate fused bead. Advances in X-Ray Analysis 41, 843–867.

Karlstrom, L., Dufek, J., Manga, M., 2009. Organization of volcanic plumbing through magmatic lensing by magma chambers and volcanic loads. Journal of Geophysical Research 114, B10204.

Kemp, A. I. S., Hawkesworth, C. J., Foster, G. L., Paterson, G. A., Woodhead, J. D., Hergt, J. M., Gray, C. M., Whitehouse, M. J., 2007. Magmatic and crustal differentiation history of granitic rocks from Hf–O isotopes in zircon. Science 315, 980–983.

Larrovere, M. A., Alasino, P. H., Baldo, E. G., 2016. La faja de cizalla dúctil doble-vergente del noroeste de la Sierra de Velasco: deformación de la corteza media durante la orogenia Famatiniana. Revista de la Asociación Geológica Argentina 73, 117–133.

López, J. P., Toselli, A. J., 1993. La faja milonıtica TIPA: faldeo oriental del Sistema de Famatina, Argentina. XII Congreso Geológico Argentino 3, 39–42.

Ludwig, K. R., 2003. Isoplot/EX version 3.0, A geochronological toolkit for Microsoft Excel: Berkeley Geochronology Center Special Publication.

Llambías, E. J., Sato, A. M., 1995. El batolito de Colangüil: transición entre orogénesis y anorogénesis. Revista de la Asociación Geológica Argentina 50, 111–131.

Macchioli Grande, M., Alasino, P. H., Rocher, S., Larrovere, M. A., Dahlquist, J. A., 2015. Asymmetric textural and structural patterns of a granitic body emplaced at shallow levels: The La Chinchilla pluton, northwestern Argentina. Journal of South American Earth Sciences 64, 58–68.

Memeti, V., Paterson, S. R., Mundil, R., 2014. Day 4: Magmatic evolution of the Tuolumne Intrusive Complex. In: Memeti, V., Paterson, S., Putrika, K. (Eds.), Formation of the Sierra Nevada Batholith: Magmatic and tectonic processes and their tempos. Geological Society of America Field guide 34, 43–54.

Michel, J., Baumgartner, L., Putlitz, B., Schaltegger, U., Ovtcharova, M., 2008. Incremental growth of the Patagonian Torres del Paine laccolith over 90 k.y. Geology 36, 459–462.

Miller, R. B., Paterson, S. R., 1999. In defense of magmatic diapirs. Journal of Structural Geology 21, 1161–1173.

Miller, R. B., Paterson, S. R., 2001. Construction of mid-crustal sheeted plutons: Examples from the North Cascades, Washington. Geological Society of America Bulletin 113, 1423–1442.

Miller, J. S., Matzel, J. E. P., Miller, C. F., Burgess, S. D., Miller, R. B., 2007. Zircon growth and recycling during the assembly of large, composite arc plutons. Journal of Volcanology and Geothermal Research 167, 282–299.

Nakamura, N., 1974. Determination of REE, Ba, Fe, Mg, Na, and K in carbonaceous and ordinary chondrites. Geochimica et Cosmochimica Acta 38, 757–775.

Pankhurst, R.J., Rapela, C. W., 1998. The proto-Andean margin of Gondwana: an introduction. In: Pankhurst, R.J., Rapela, C.W. (Eds.), The proto-Andean margin of Gondwana. Geological Society of London, Special Publications 142, 1–9.

Paterson, S. R., 2009. Magmatic tubes, pipes, troughs, diapirs, and plumes: Late-stage convective instabilities resulting in compositional diversity and permeable networks in crystal-rich magmas of the Tuolumne batholith, Sierra Nevada, California. Geosphere 5, 496–527.

Paterson, S. R., Vernon, R. H., 1995. Bursting the bubble of ballooning plutons: A return to nested diapirs emplaced by multiple processes. Geological Society of America Bulletin 107, 1356–1380.

Paterson, S. R., Onezime, J., Teruya, L., Žák, J., 2003. Quadruple-pronged enclaves: their significance for the interpretation of multiple magmatic fabrics in plutons. Journal of the Virtual Explorer 10.

Paterson, S., Farris, D., 2008. Downward host rock transport and the formation of rim monoclines during the emplacement of Cordilleran batholiths. Transactions of the Royal Society of Edinburgh: Earth Sciences 97, 397–413.

Paterson, S. R., Memeti, V., Mundil, R., Žák, J., 2016. Repeated, multiscale, magmatic erosion and recycling in an upper crustal pluton: implications for magma chamber dynamics and magma volume estimates. American Mineralogist (in press).

Petford, N., Cruden, A. R., McCaffrey, K. J. W., Vigneresse, J. L., 2000. Granite magma formation, transport and emplacement in the Earth's crust. Nature 408, 669–673.

Pinotti, L. P., D'Eramo, F. J., Weinberg, R. F., Demartis, M., Tubía, J. M., Coniglio, J. E., Radice, S., Maffini, M. N., Aragón, E., 2016. Contrasting magmatic structures between small plutons and batholiths emplaced at shallow crustal level (Sierras de Córdoba, Argentina). Journal of Structural Geology 92, 46–58.

Rapela, C. W., Baldo, E. G., Pankhurst, R. J., Fanning, C. M., 2008b. The Devonian Achala batholith in the Sierras Pampeanas: F-rich aluminous A-type granites. VI South American Symposium on Isotope Geology, Proceedings in CD-ROM, Paper 53. San Carlos de Bariloche, Argentina. 8 pp.

Read, H. H., 1962. Donegal as a natural laboratory for metamorphic geology. S. K. Roy Commemoration Bulletin of the I. S. M. Geological Society, Indian School of Mines. Dhanbad, 9–13.

Rittmann, A., 1957. On the serial character of igneous rocks. Egyptian Journal of Geology

1, 23–48.

Rossi, J. N., Toselli, A. J., López, J. P., 1999. Deformación y metamorfismo en el NW de la sierra de Velasco, La Rioja, Argentina. Zentralblatt für Geologie und Paläontologie I 7/8 839–850.

Saleeby, J. B., 1990. Progress in tectonic and petrogenetic studies in an exposed cross-section of young (ca. 100 Ma) continental crust, southern Sierra Nevada, California. In: Salisbury, M. H., Fountain, D. M., (Eds.), Exposed cross-sections of the continental crust. Amsterdam, Netherlands, Kluwer Academic, NATO Advanced Studies Institute, p. 137–158.

Sato, K., Basei, M. A. S., Ferreira, C. M., Vlach, S. R. F., Ivanuch, W., Siga Jr., O., Onoi, A. T., 2010. In situ U-Th-Pb isotopic analyses by Excimer laser ablation/ICP–MS on Brazilian xenotime megacrystal: first U-Pb results at CPGeo-IG-USP. VII South American Symposium on Isotope Geology, CD Room. Brasília, DF.

Sato, K., Basei, M. A. S., Ferreira, C. M., Sproesser, W. M., Vlach, S. R. F., Ivanuch, W., Onoi, A. T., 2011. U-Th-Pb analyses by excimer laser ablation / ICP-MS on MG Brazilian xenotime. Goldschmidt Conference Abstracts, p. 1801.

Schmeling, H., Cruden, A. R., Marquart, G., 1988. Deformation in and around a fluid sphere moving through a viscous medium: implications for diapiric ascent. Tectonophysics 149, 17–34.

Schulmann, K., Ježek, J., Venera, Z., 1997. Perpendicular linear fabrics in granite: markers of combined simple shear and pure shear flows? In: Bouchez, J. L., Hutton, D., Stephens, S. (Eds.), Granite: From Segregation of Melt to Emplacement Fabrics. Kluwer Academic Publisher, Dordrecht, pp. 159–176.

Tomek, F., Žák, J., Chadima, M., 2014. Magma flow paths and strain patterns in magma chambers growing by floor subsidence: a model based on magnetic fabric study of shallow-level plutons in the Štiavnica volcano–plutonic complex, Western Carpathians. Bulletin of Volcanology 76, 873.

Tornare, E., Pilet, S., Bussy, F., 2016. Magma differentiation in vertical conduits revealed by the complementary study of plutonic and volcanic rocks from Fuerteventura (Canary Islands). Journal of Petrology 57, 2221–2250.

Toselli, A. J., Rossi, J. N., Basei, M. A. S., Larrovere, M., 2011. Controles geoquímicos e isotópicos en la petrogénesis de los granitos Devónico-Carboníferos Santa Cruz y Asha: Sierra de Velasco, Argentina. Serie Correlación Geológica 27, 77–98.

Vaughan, A. P. M., Pankhurst, R. J., 2008. Tectonic overview of the West Gondwana margin. Gondwana Research 13, 150–162.

Vernon, R. H., Etheridge, M. A., Wall, V. J., 1988. Shape and microstructure of microgranitoid enclaves: indicators of magma mingling and flow. Lithos 22, 1–11.

Whalen, J. B., Currie, K. L., Chappell, B. W., 1987. A-type granites: geochemical characteristics, discrimination and petrogenesis. Contributions to Mineralogy and Petrology 95, 407–41

Willis, D. G., 1977. A kinematic model of preferred orientation. Geological Society of America Bulletin 88, 883–894.

Wilson C. J. N., Charlier, B. L. A., 2016. The life and times of silicic volcanic systems. Elements 12, 103–108.

Wilson, M., 1989. Igneous Petrogenesis, A Global Tectonic Approach. Unwin Hyman, London, p. 466.

Yoshinobu, A. S., Okaya, D. A., Paterson, S. R., 1998. Modeling the thermal evolution of fault-controlled magma emplacement models: implications for the solidification of granitoid plutons. Journal of Structural Geology 20, 1205–1218.

Yoshinobu, A. S., Fowler Jr, T. K., Paterson, S. R., Llambias, E., Tickyj, H., Sato, A. M., 2003. A view from the roof: magmatic stoping in the shallow crust, Chita pluton, Argentina. Journal of Structural Geology 25, 1037–1048.

Žák, J., Paterson, S. R., Memeti, V., 2007. Four magmatic fabrics in the Tuolumne batholith, central Sierra Nevada, California (USA): implications for interpreting fabric patterns in plutons and evolution of magma chambers in the upper crust. Geological Society of America Bulletin 119, 184–201.

Figure captions

Figure 1. Simplified geological maps of NW Argentina: (a) Sierras Pampeanas; (b) Sierra de Velasco. Map (a) shows the boundary of the Carboniferous-Permian Paganzo basin. In (a) index map shows location of the Sierras Pampeanas in Argentina. In (b) box shows location of present study (see Fig. 2).

Figure 2. Image of the northern Sierra de Velasco showing the overall structure and composition of the basement block. The smooth western flank represents an ancient regional-scale erosion surface known as the Pampean peneplain (Jordan et al., 1989). At the base of the western flank, Miocene continental strata are gently tilted (12-15 degrees), dipping towards the NW.

Figure 3. Map showing structural data from the main igneous units of the San Blas intrusive complex (SBIC) and their host rocks. The different types of magmatic foliations in the SBIC are classified based on the orientation.

Figure 4. (a) Intrusive contacts between granitoids of the San Blas unit and the host rock (mylonite). The metamorphic foliation is roughly concordant to the contact. (b) Floor contact between the Asha igneous unit (on top) and mylonite. (c) Intrusive contact between Asha (on the top) and San Blas units. (d) Intrusive contact in mingling relationship between San Blas and Hualco units. Some granitoid blocks of the San Blas unit are included in the Hualco unit.

Figure 5. Restoration of cross-sections of different places of the San Blas intrusive complex. (A, B and C) Floor contact between the Asha igneous unit (on top) and mylonite. (D, E, F, G, H and I) Roof contact between the Asha and San Blas igneous units. (J) Roof contact between the San Blas and Hualco igneous units.

Figure 6. (a) Cognate inclusions of older parts of the SBIC in granitoids of the San Blas units. (b) Two perpendicularly oriented enclaves in the Hualco unit, the small inclusion is ~N-S and the biggest one is oriented ~E-W but with prongs parallel to the first one. (c) Steeply dipping NNW-SSE magmatic foliation (type A_1) in the northern part of the Asha unit. The ruler has 15 cm long. (d) Two steeply dipping magmatic foliations (type 2 and 1) defined by alignment of K-feldspar phenocrysts in the central part of the San Blas unit. Type 1 overprints type 2.

Figure 7. Contour map of the structures in the San Blas intrusive complex. Lines indicate the trajectory foliations and their dip directions. Note how contour lines of type SB_2 are disposed around the HU intrusion. Stereonets (equal-area, lower-hemisphere projections) show orientations of different magmatic foliations and enclaves for the main igneous units.

Figure 8. (a) Total alkali vs. silica variation diagram for the SBIC. The alkaline / mid-alkaline / subalkaline magmatic lineages are defined by sigma isopleths (after Rittmann, 1957). The grey field represents 45 Carboniferous granitic samples of the Sierra de Velasco and Sierra de Fiambalá (Dahlquist et al., 2010); (b, c) classification diagrams of Frost et al. (2001): (a) $FeO^t/(FeO^t+MgO)$ vs. SiO_2 and (b) Na_2O+K_2O-CaO vs. SiO_2. The A-type granite field is after Frost et al. (2001); and (d, e, f) chondrite-normalized (after Nakamura, 1974) REE plots of samples of the main igneous units of the SBIC.

Figure 9. U–Pb LA-MC-ICP-MS zircon dating of the samples a) ASH-8 (Asha unit), b) SB-10 (San Blas unit) and c) HUAL-9 (Hualco unit) from the SBIC. Selected zircon images are also shown. Data are reported in Table 2.

Figure 10. Average εHf_t isotope composition of melt-precipitated zircons from samples of each unit as a function of whole-rock εNd_t isotope composition at the time of crystallization of the granitic rocks of the SBIC. References: (1) Early-Middle Ordovician rocks, (2) Middle-Late Devonian rocks, and (3) Early Carboniferous rocks (data taken from Dahlquist et al., 2013).

Figure 11. Interpretive block-diagrams illustrating the evolution in the emplacement styles of the main igneous units of the SBIC. (a) Location of the block-diagram in the Sierra de Velasco. (b) Intrusion of the magmas of the Asha unit, with piecemeal floor subsidence of multiple host-rock blocks as the main emplacement mechanism. (c, d) Intrusion of the magmas of the San Blas unit rising as elongated bodies with host rock deformation by both brittle and ductile processes. An amount of calculated shortening up to 30 % in the host rock occurred by the pushing of the SBU intrusion. (e) Intrusion of the magmas of the Hualco unit into the San Blas unit with a dominant host rock deformation by ductile processes.

Figure 12. Crystal size distribution analyses of seven field photographs show two crystals populations belonging to the two respective main foliation planes. Photographs: (a, b) Asha unit, (c, d, e) San Blas unit, and (f, g) Hualco unit. (h) Population density curves of the considered magmatic foliations in this study. All curves share a characteristic shape, with an exponential decrease in the number of larger crystals, from 22 to 75 mm, and an exponential drop below 19 mm.

Figure 13. Compilation of the zircon ages obtained to the igneous units of the San Blas Intrusive complex. A maximum value of 6 m.y. for the construction of the SBIC is defined between the older and younger ages. This value may be biased toward the youngest phases of plutonism, where most of the grains that yield older ages are in the youngest igneous units.

Figure 14. (a, b, c) Conceptual model for the generation of the magmas of the SBIC showing the evolution of the multiple batches assembled incrementally into upper crust. See text for discussion.

Figure 1

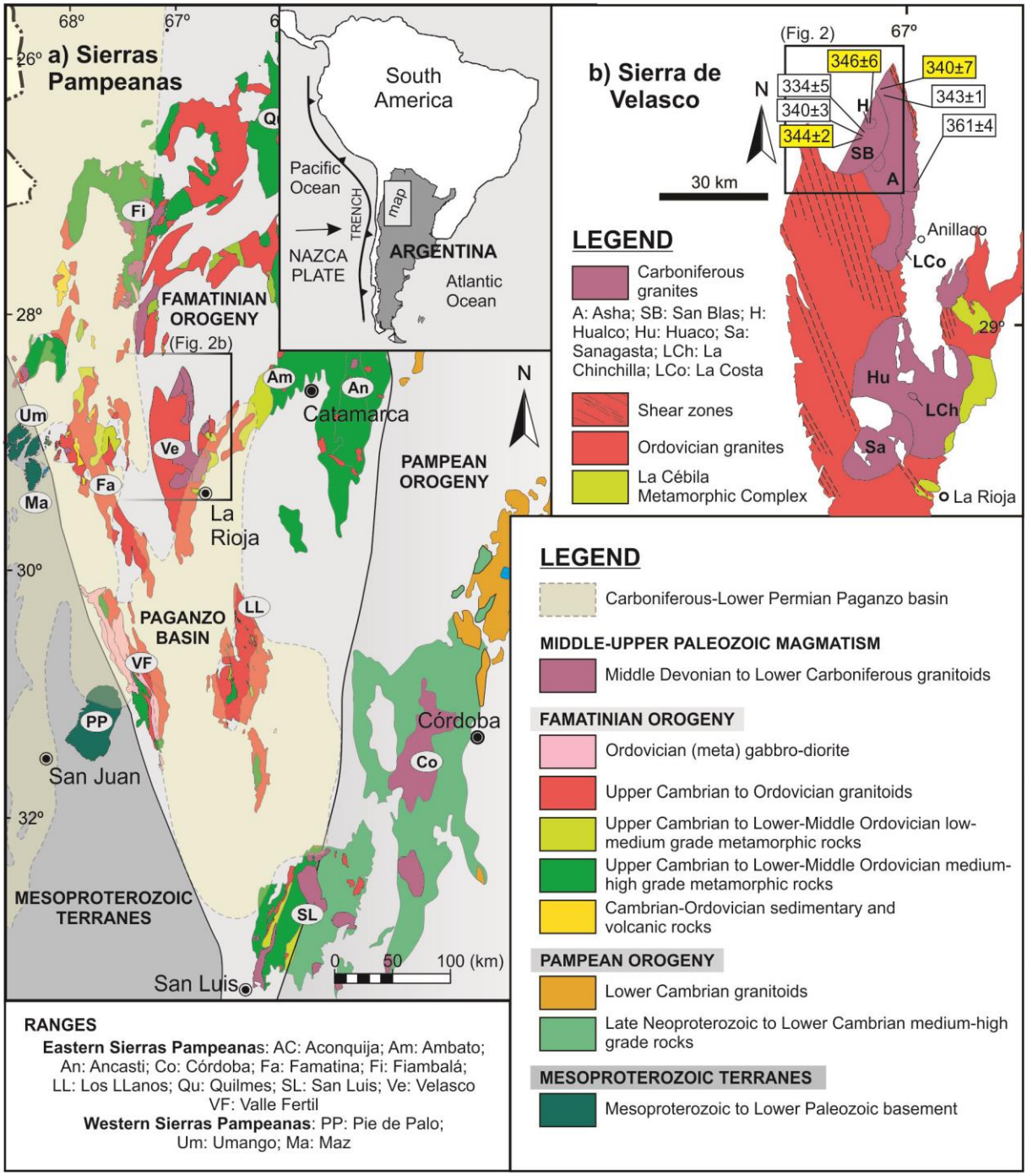

Figure 2

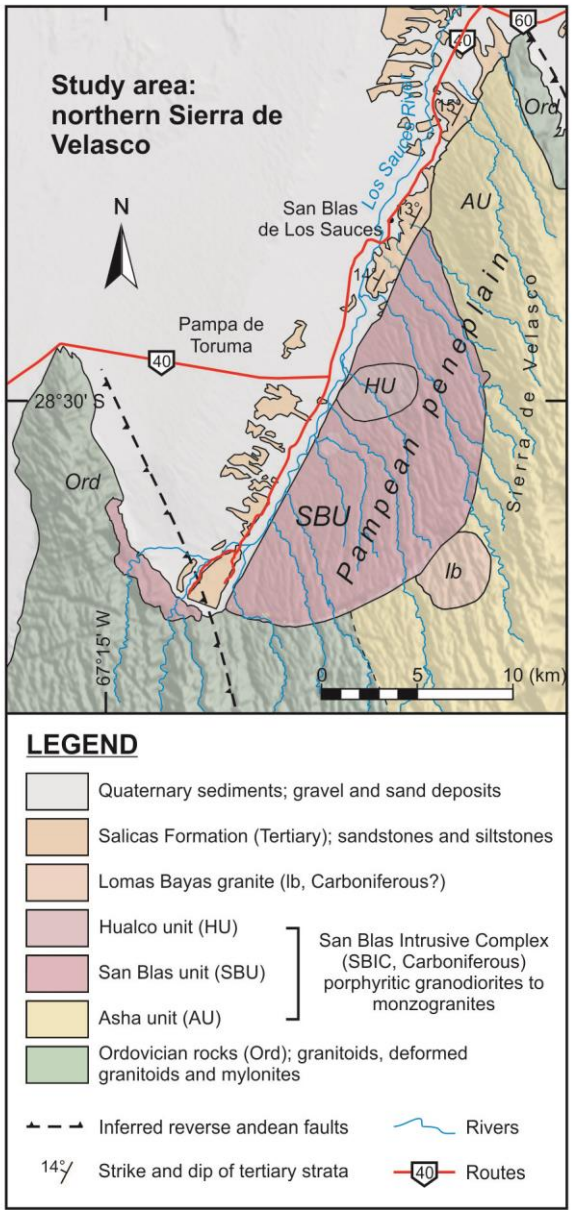

Figure 3

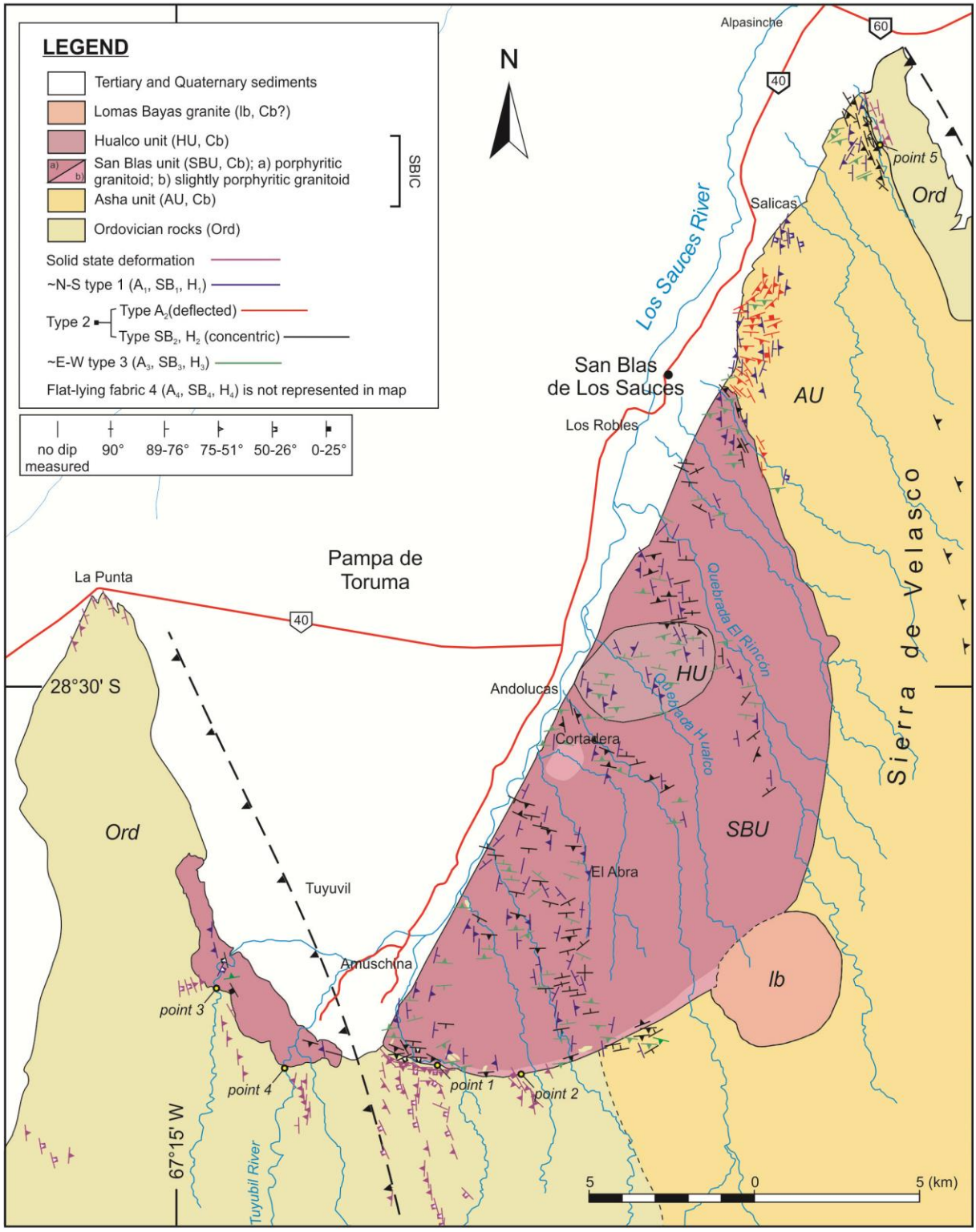

Figure 4

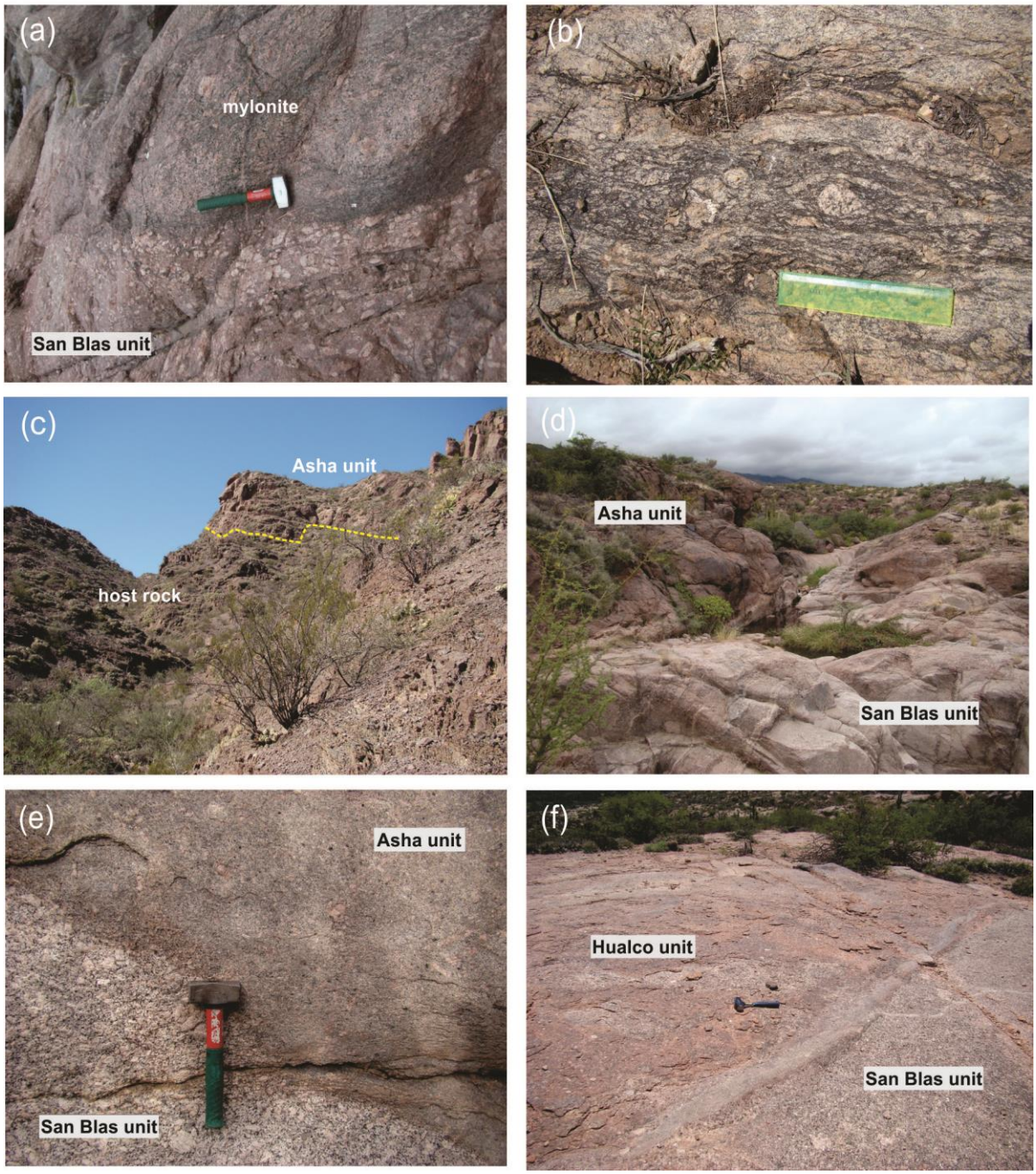

Figure 5

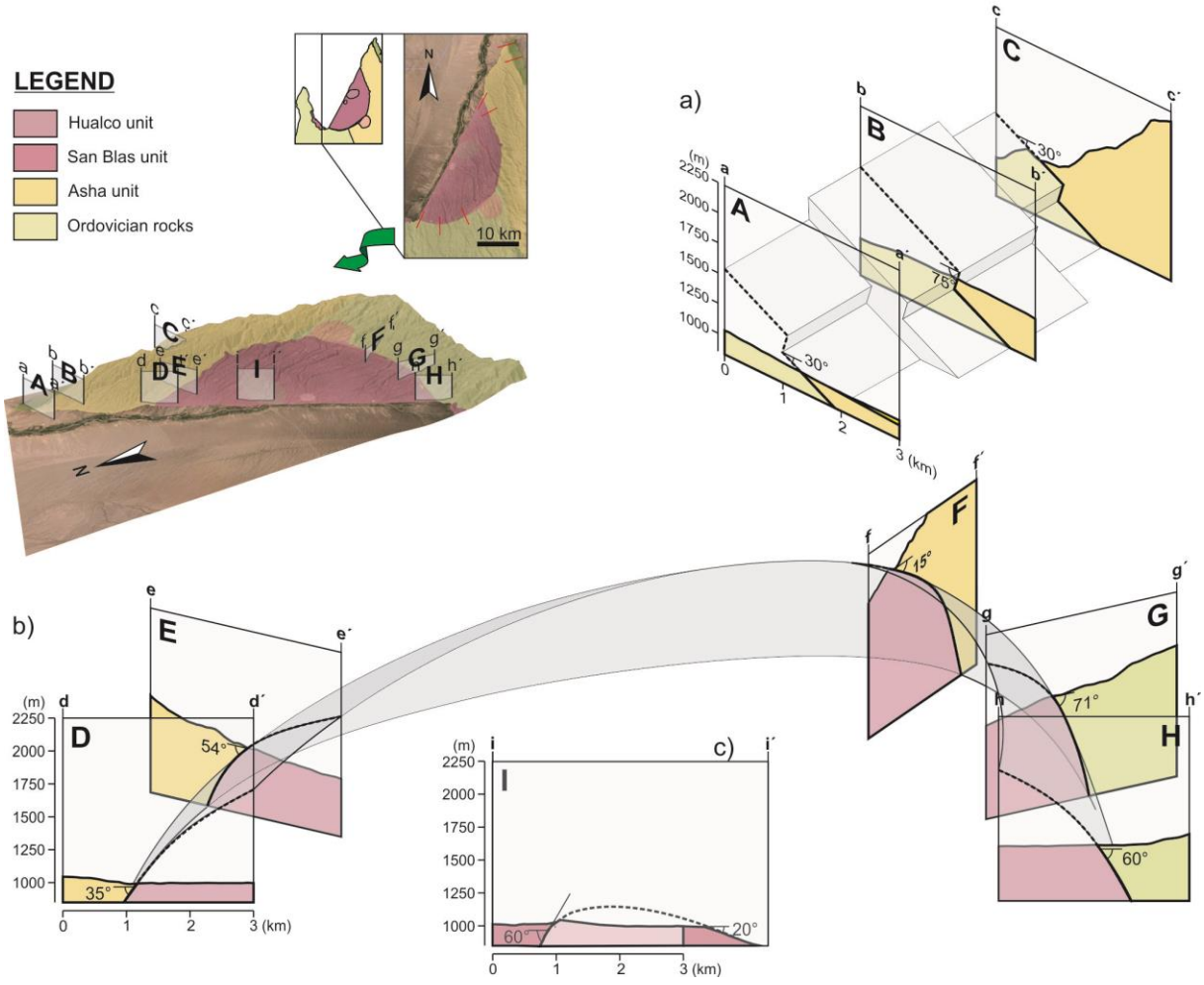

Figure 6

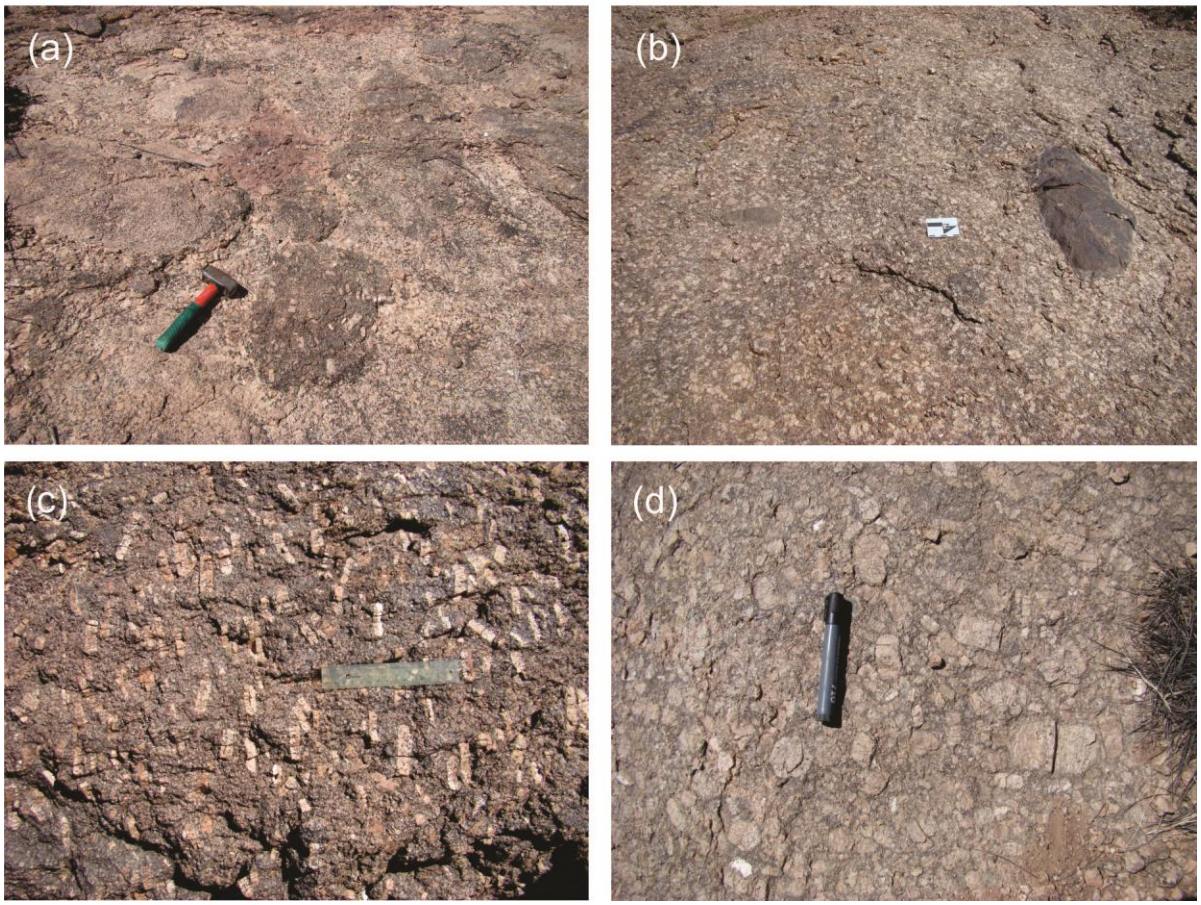

Figure 7

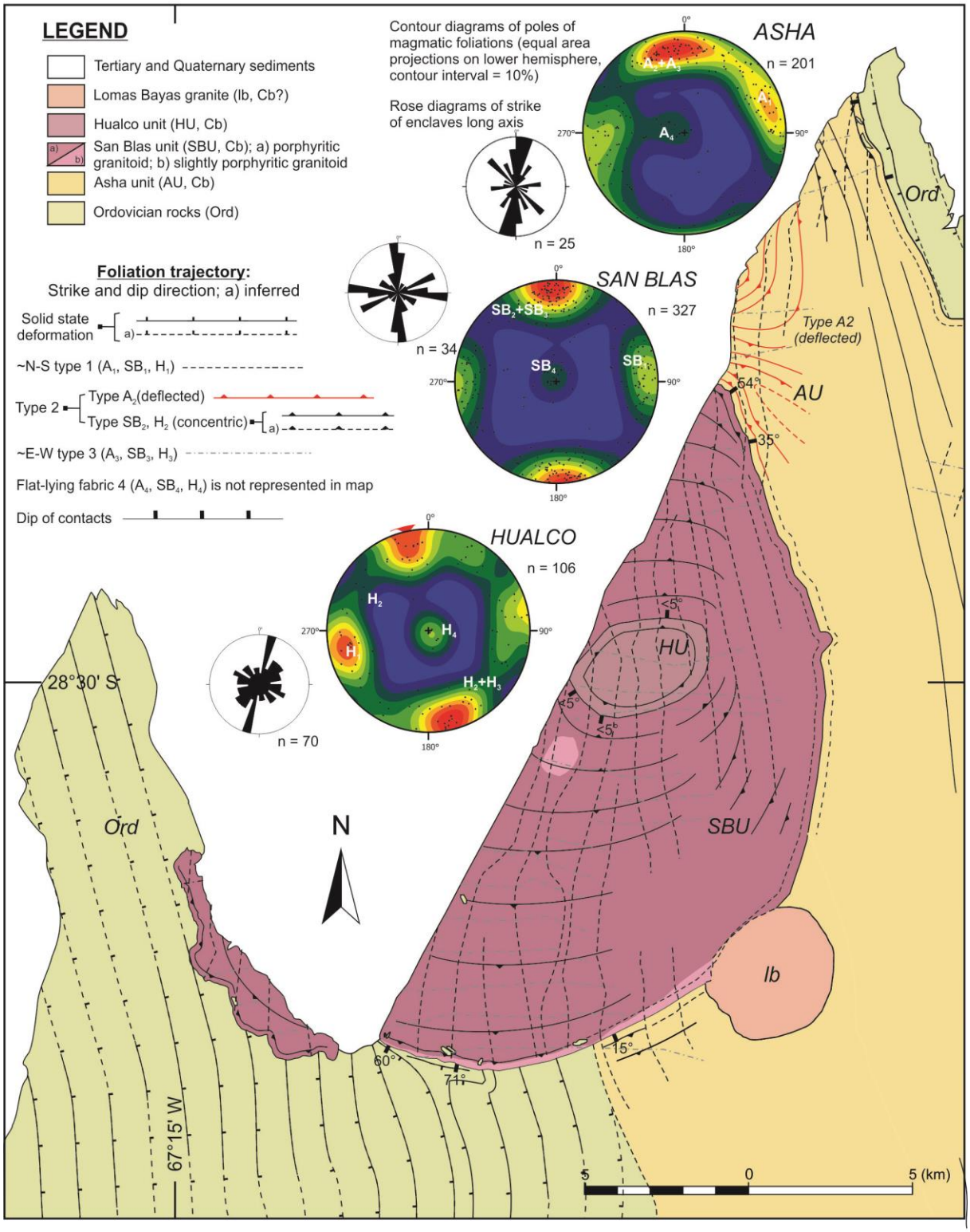

Figure 8

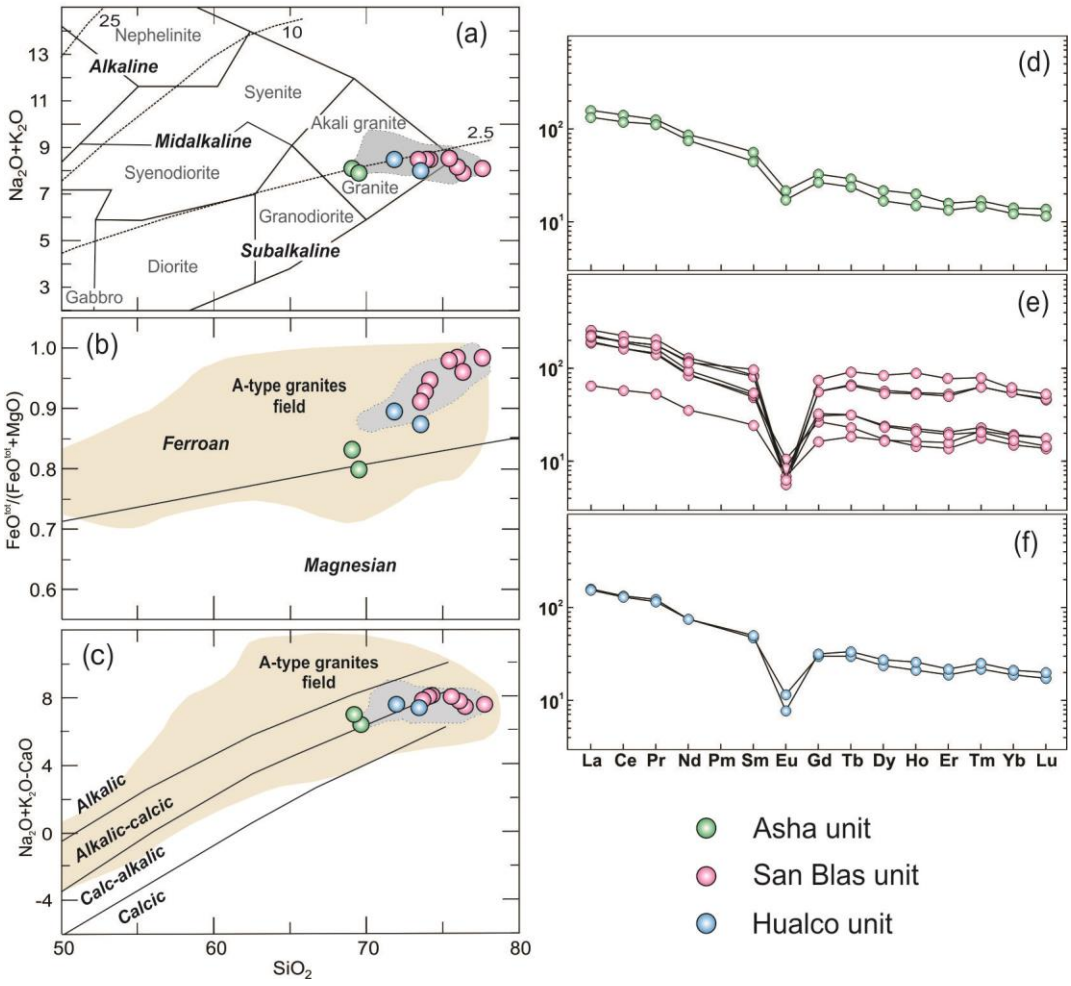

Figure 9

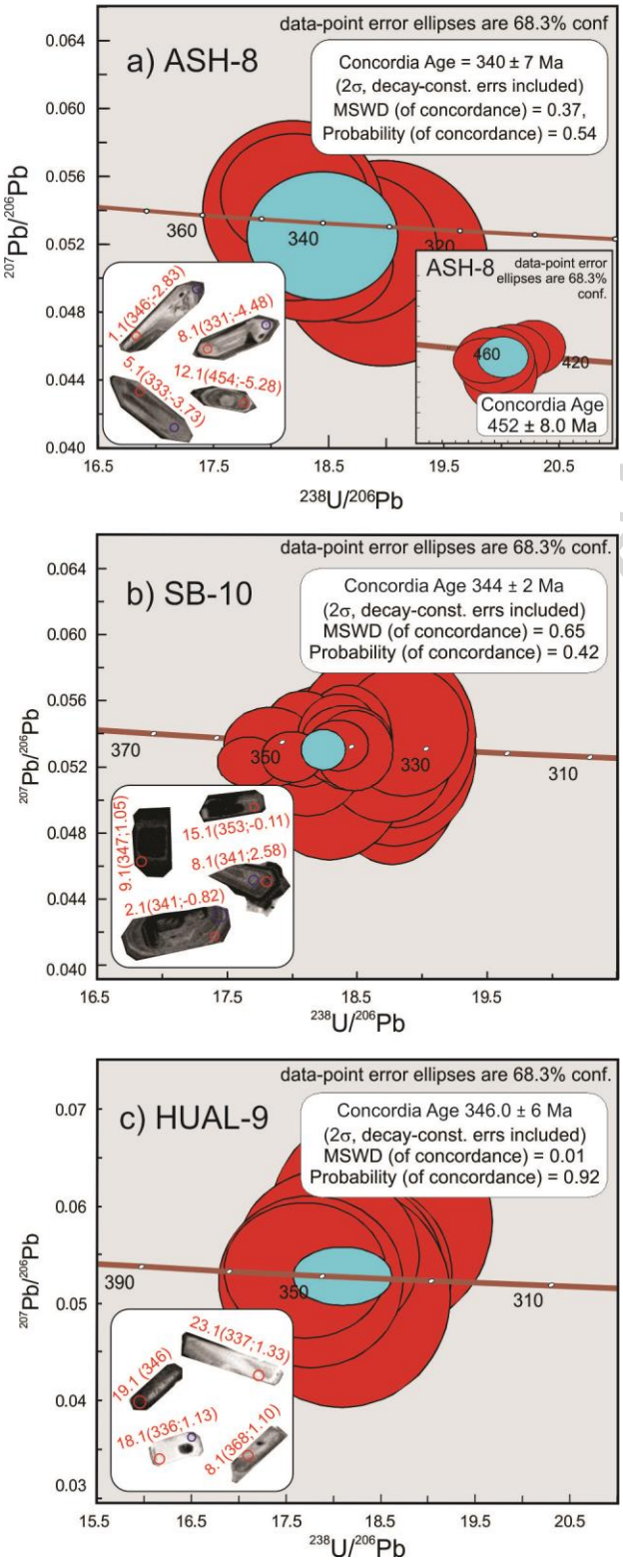

Figure 10

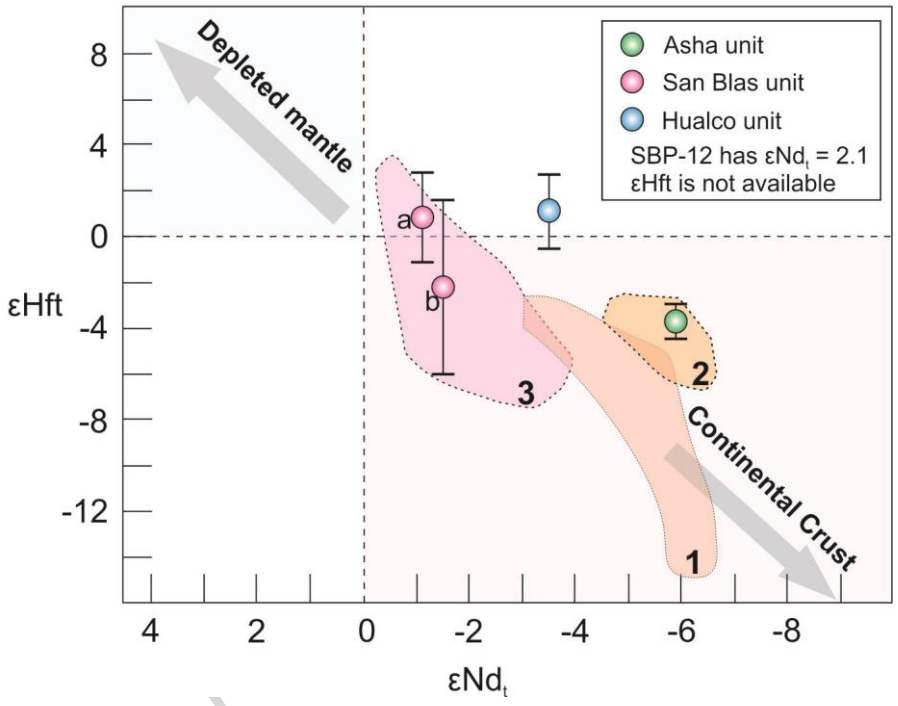

Figure 11

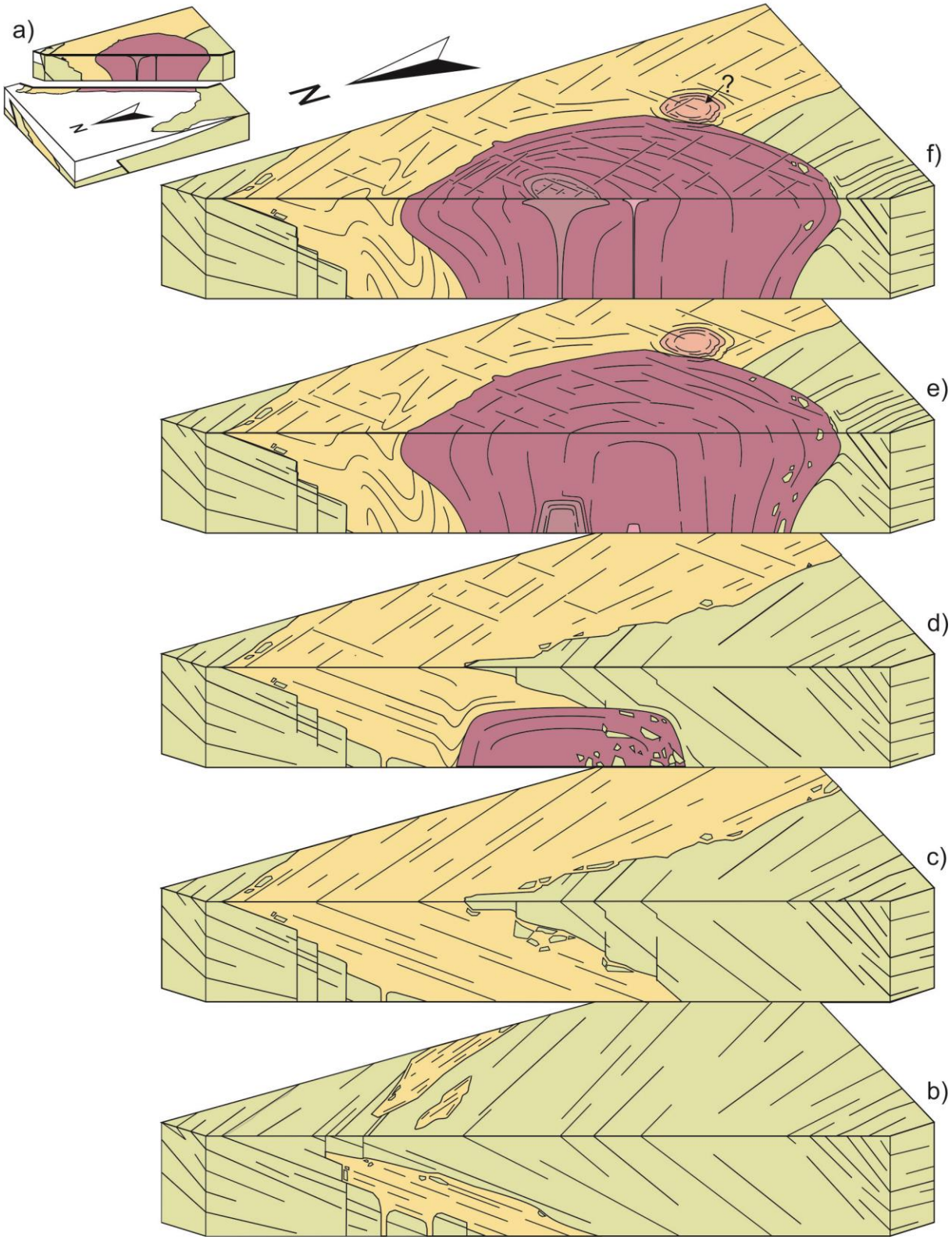

Figure 12

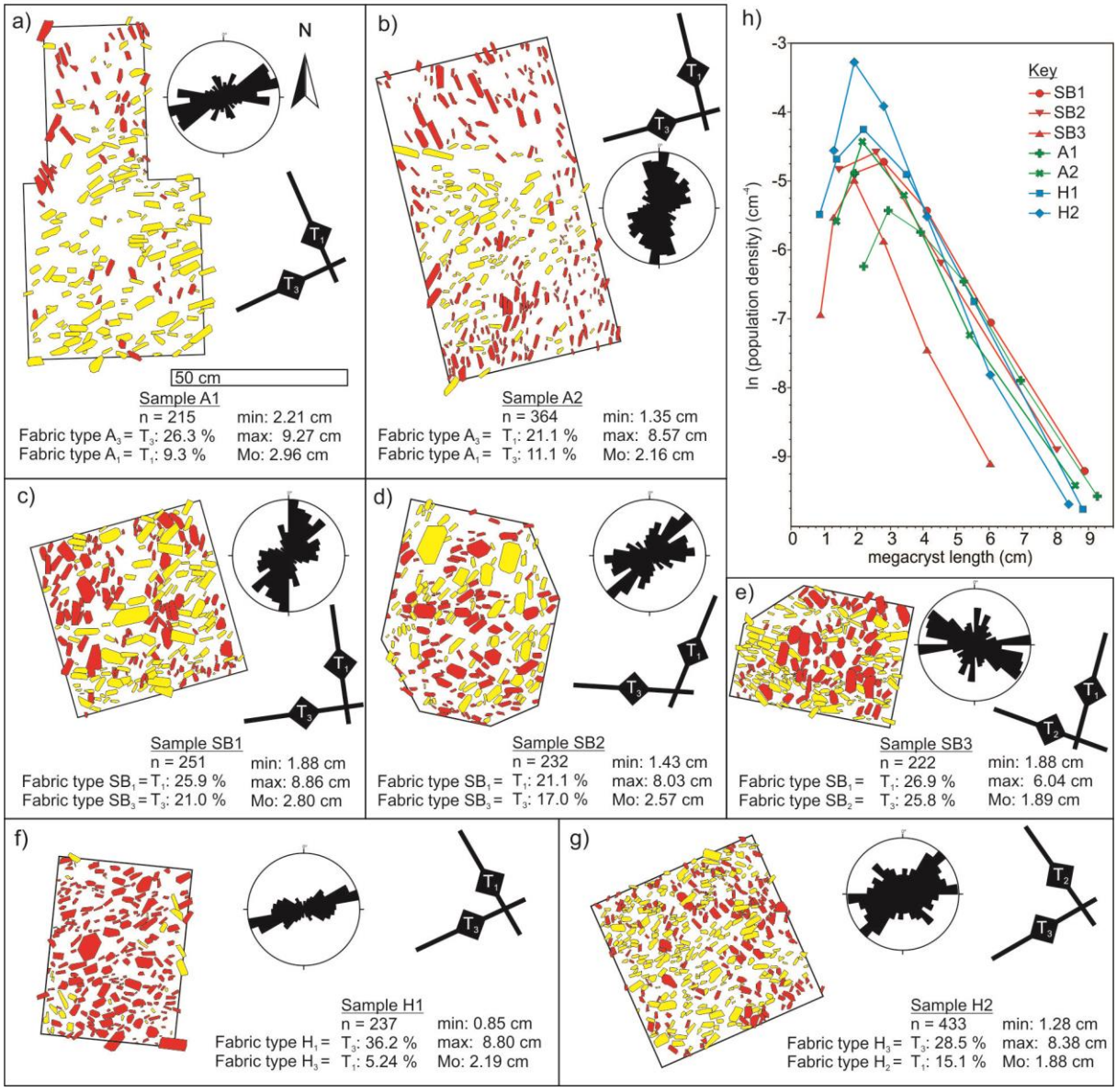

Figure 13

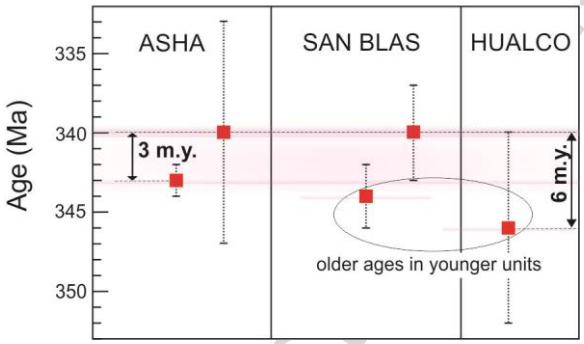

Figure 14

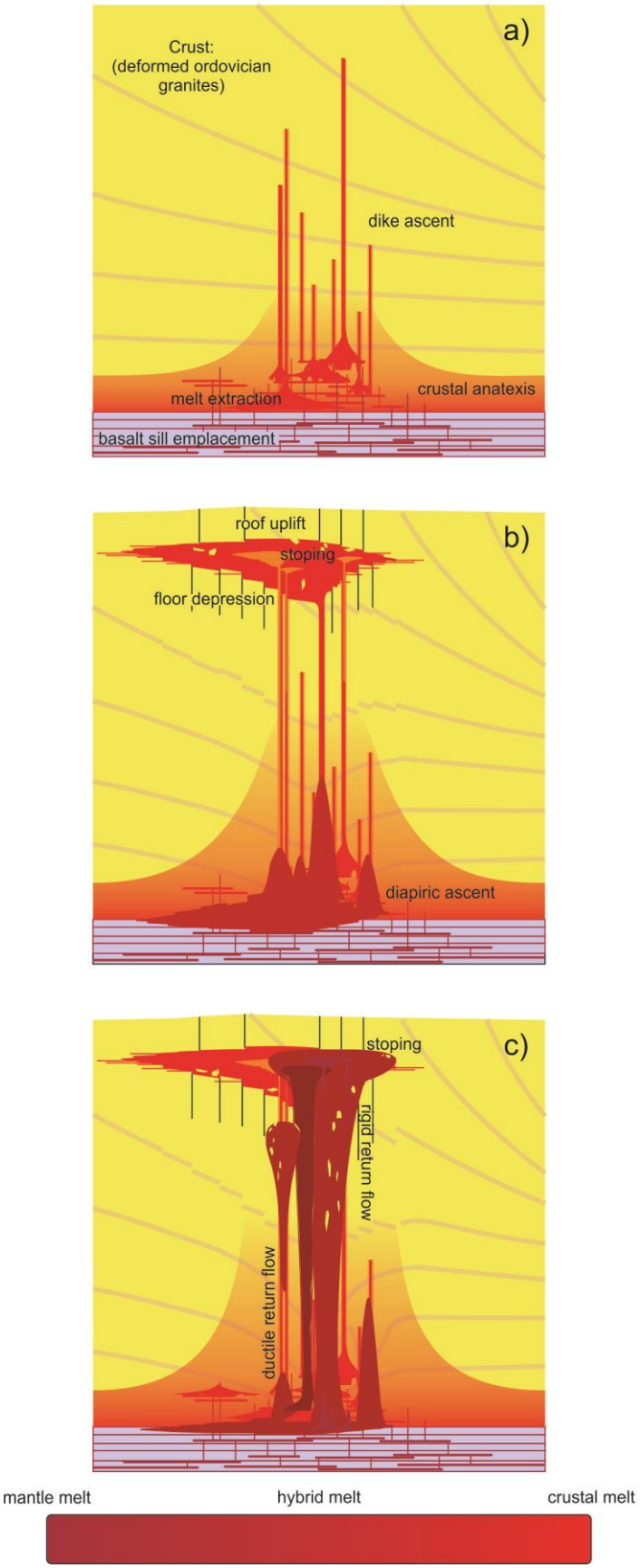

Table 1. Major and trace element compositions of the dated samples from the SBIC

Unit	Asha	San Blas	Hualco
Sample	ASH-8	SB-10	HUAL-9
wt.%			
SiO_2	68.61	76.34	72.58
TiO_2	0.72	0.10	0.28
Al_2O_3	14.57	11.61	14.05
FeO^t	3.66	1.38	2.24
MnO	0.09	0.02	0.06
MgO	0.92	0.03	0.33
CaO	1.76	0.72	0.79
Na_2O	2.97	3.15	3.34
K_2O	4.99	4.97	4.74
P_2O_5	0.35	0.02	0.26
LOI(%)	0.69	0.50	0.91
ppm			
Cs	29	16	64
Rb	308	484	519
Sr	116	17	37
Ba	445	48	122
La	52.1	74.5	51.0
Ce	121	169	112
Pr	14.2	20.0	13.1
Nd	54.8	73.5	47.1
Sm	11.5	19.5	10.2
Eu	1.66	0.48	0.59
Gd	8.93	20.7	8.62
Tb	1.38	4.33	1.56
Dy	7.49	29.2	9.46
Ho	1.40	6.24	1.83
Er	3.61	17.2	4.94
Tm	0.51	2.39	0.75
Yb	3.11	13.2	4.66
Lu	0.46	1.80	0.69
U	3.80	16.9	5.93
Th	27.9	104	33.7
Y	36.0	160	49.2
Nb	22.4	137	49.7

Zr	253	278	181
Hf	6.81	11.2	5.75
Ta	2.50	6.68	7.86
Ga	22	28	24
Ga/Al*	2.79	4.5	3.22

Total iron expressed as FeO^{total} Ga/Al*

= 10.000*Ga/Al

Table 2. LA-MC-ICP-MS zircon results for the main igneous units from the SBIC

ASHA UNIT. sample ASH-8		Isotopic Ratios				Ages (Ma)			
Spot	GCh SS	238/206	1 sigma	207/206	1 sigma	206/238	1 sigma	207/206	1 sigma
1.1	e, p, osc	18.1971	0.5168	0.0540	0.0035	345	10	370	142
4.1	e, p, hb	18.7307	0.4735	0.0518	0.0029	335	8	277	131
8.1	e, p, hb	18.9788	0.6009	0.0509	0.0040	331	10	238	164
11.1	e, p, osc	18.2087	0.4220	0.0549	0.0024	345	8	409	98
24.1	e, p, hb	18.3786	0.4550	0.0508	0.0022	342	8	231	100
Inherited ages									
3.1	m, p, hd	14.2119	0.3191	0.0568	0.0023	438	10	485	92
7.1	ic, p, hb	13.7080	0.3704	0.0535	0.0033	454	12	351	135
12.1	e, p, osc	13.6924	0.2868	0.0559	0.0020	454	9	449	80
19.1	e, p, osc	13.4853	0.3173	0.0551	0.0019	461	10	415	79
20.1	e, p, hb	13.6569	0.3097	0.0556	0.0020	456	10	438	82
23.1	m, p, osc	13.6295	0.3976	0.0551	0.0028	456	13	415	109
25.1	m, p, hb	13.8927	0.3740	0.0558	0.0026	448	12	446	102
SAN BLAS UNIT. sample SB-10									
2.1	e, p, osc	18.3547	0.2116	0.0537	0.0018	342	4	358	78
5.1	e, p, hb	18.4225	0.2237	0.0538	0.0021	341	4	363	90
6.1	e, p, hd	17.9936	0.1550	0.0526	0.0010	349	3	314	41
7.1	e, p, hb	18.7637	0.3642	0.0523	0.0041	335	6	300	165
8.1	e, p-fr, osc	18.4737	0.1970	0.0530	0.0016	340	4	329	67
9.1	e, p, hd	18.3499	0.1559	0.0533	0.0010	342	3	341	42
10.1	e, p, osc	17.6598	0.1593	0.0523	0.0010	355	3	297	45
12.1	e, p, hd	18.0805	0.2159	0.0537	0.0019	347	4	359	79
15.1	e, p, hb	17.8276	0.2390	0.0532	0.0016	352	5	337	70

16.1	e, p, hb	18.1078	0.2761	0.0522	0.0021	347	5	296	86
17.1	e, p-fr, hb	18.7962	0.4022	0.0538	0.0036	334	7	363	147
18.1	e, p, osc	18.4145	0.2292	0.0536	0.0014	341	4	354	60
22.1	e, p, osc	18.7808	0.4126	0.0527	0.0036	334	7	315	135
23.1	e, p, osc	18.5476	0.3345	0.0543	0.0028	339	6	384	117
24.1	e, p, hb	18.7282	0.3275	0.0526	0.0026	335	6	314	106
25.1	e, p, osc	18.2809	0.3875	0.0517	0.0035	343	7	274	148
26.1	e, p, osc	18.8542	0.3243	0.0542	0.0026	333	6	379	110
HUALCO UNIT. sample HUAL-9									
1.1	e, p, hd	17.8305	0.4224	0.0533	0.0021	352	8	344	90
2.1	e, p-fr, osc	18.2680	0.6617	0.0538	0.0062	344	12	363	236
3.1	e, p, osc	17.7421	0.5524	0.0541	0.0045	353	11	377	182
6.1	e, p, hb	18.1744	0.6752	0.0534	0.0066	345	12	346	245
8.1	e, p-fr, hb	17.8072	0.6317	0.0530	0.0057	352	12	329	239
9.1	e, p, osc	18.0358	0.5203	0.0534	0.0037	348	10	344	158
10.1	e, p, osc	17.9858	0.6265	0.0556	0.0057	349	12	436	225
11.1	e, p-fr, osc	18.5008	0.5871	0.0547	0.0045	339	10	398	190
19.1	e, p, hd	18.5340	0.3995	0.0532	0.0014	339	7	336	061
23.1	e, p, hb	18.5282	0.7703	0.0591	0.0074	339	14	572	231
26.1	e, p, hb	18.1308	0.7452	0.0515	0.0074	346	14	262	213

$^{238}U/^{206}Pb$ and $^{207}Pb/^{206}Pb$ ratios corrected for static fractionation using GJ 1.

Measurement errors represent within-run uncertainty only. Grain characteristics (GCh) and site of the spot (SS): CL images: osc = oscillatory zoning, hb = homogeneous bright, hd = homogenous dark. Site of the spot: e = end or edge. Habit of the grain: p = prism. fr = fragmented.

Table 3. Laser ablation Hf isotope data for igneous dated zircons from ASH-8, SB-10 and HUAL-9 of the SBIC.

Grain/spot	$^{176}Hf/^{177}Hf$	± 2 s	$^{176}Lu/^{177}Hf$	± 2 s	$^{176}Hf/^{177}Hf_{(t)}$	$\varepsilon Hf_{(t)}$	T_{DM} (Ga)
ASHA UNIT (t_1)							
1.1	0.282489	0.000058	0.001191	0.000046	0.282481	-2.8	1.47
4.1	0.282461	0.000041	0.000977	0.000009	0.282455	-3.9	1.53
11.1	0.282462	0.000061	0.001194	0.000035	0.282454	-3.8	1.53
9.1	0.282487	0.000066	0.001431	0.000010	0.282478	-2.9	1.48
8.1	0.282444	0.000054	0.001490	0.000023	0.282435	-4.5	1.58
3.1*[1]	0.282397	0.000052	0.002924	0.000032	0.282373	-4.2	1.64
12.1*[1]	0.282368	0.000053	0.003129	0.000040	0.282341	-5.3	1.71
23.1*[1]	0.282399	0.000047	0.002311	0.000050	0.282379	-3.9	1.63
3.1*[2]	0.282397	0.000052	0.002924	0.000032	0.282373	-6.5	1.64
12.1*[2]	0.282368	0.000053	0.003129	0.000040	0.282341	-7.6	1.71

23.1*[2]	0.282399	0.000047	0.002311	0.000050	0.282379	-6.3	1.63
SAN BLAS UNIT (t_2)							
2.1	0.282543	0.000032	0.001307	0.000034	0.282534	-0.8	1.35
5.1	0.282561	0.000048	0.001117	0.000044	0.282554	-0.1	1.31
6.1	0.282648	0.000067	0.001755	0.000012	0.282637	2.8	1.12
7.1	0.282584	0.000048	0.001289	0.000030	0.282576	0.6	1.26
8.1	0.282637	0.000047	0.000930	0.000008	0.282631	2.6	1.13
9.1	0.282602	0.000055	0.002213	0.000031	0.282587	1.0	1.23
12.1	0.282568	0.000053	0.000989	0.000033	0.282561	0.1	1.29
15.1	0.282559	0.000041	0.000682	0.000002	0.282555	-0.1	1.30
17.1	0.282534	0.000066	0.001248	0.000020	0.282526	-1.1	1.37
18.1	0.282635	0.000055	0.001356	0.000032	0.282627	2.4	1.14
22.1	0.282577	0.000045	0.000788	0.000008	0.282572	0.5	1.26
HUALCO UNIT (t_3)							
8.1	0.282648	0.00007	0.000811	0.000031	0.282643	3.0	1.10
18.1	0.282637	0.00008	0.000780	0.000006	0.282632	2.7	1.13
23.1	0.282548	0.00007	0.000825	0.000007	0.282542	-0.5	1.33

Laser operating conditions: GJ1 - 6mJ ou 8.55J/cm2 (100%). 7Hz.spot = 47um. He (MCF1) = 0.25l/min (MCF2)= 0.5L/min. N2 = 1.2mL/min. 50 cycles. AR80=30V.

t = crystallization age (t_1 = 340 Ma for Asha unit; t_2 = 344 Ma for San Blas unit and t_3 = 346 Ma for Hualco unit). T_{DM} = depleted mantle model age.

Present CHUR day is $^{176}Hf/^{177}Hf$ = 0.282772 and $^{176}Lu/^{177}Hf$ = 0.0332 (Blichert-Toft and Albarede, 1997) $^{176}Hf/^{177}Hf_{CHUR(t1)}$ = 0.282562; $^{176}Hf/^{177}Hf_{CHUR(t2)}$ = 0.282558; $^{176}Hf/^{177}Hf_{CHUR(t3)}$ = 0.282557 *Inherited zircon crystal: *[1]Calculated to 452 Ma, $^{176}Hf/^{177}Hf_{CHUR(t=452)}$ = 0.282491; *[2]Calculated to 338 Ma.

T_{DM} = A two–stage continental model (T_{DM2}) was calculated using the initial $^{176}Hf/^{177}Hf$ of zircon and the $^{176}Lu/^{177}Hf$=0.022 ratio for the lower continental crust (Griffin et al., 2004).

Table 4. Rb-Sr and Sm-Nd data for igneous samples from the SBIC.

Sample	Rb (ppm)	Sr (ppm)	$^{87}Rb/^{86}Sr$	$^{87}Sr/^{86}Sr$	$^{87}Sr/^{86}Sr_{(t)*}$	Sm (ppm)	Nd (ppm)	$^{147}Sm/^{144}Nd$	$^{143}Nd/^{144}Nd$	$^{143}Nd/^{144}Nd_{(t)}$	$\varepsilon Nd_{(t)}$ [†]	TDM[§]
Granite												
ASH-8	513	38	7.571	0.76105	0.72440	11.4	54.7	0.126	0.51218	0.51189	-5.9	1.49
SB-10	484	17	86.19	1.18144	0.76431	19.4	73.4	0.160	0.51250	0.51214	-1.1	1.51
HUAL-9	513	38	40.06	0.96992	0.77604	10.2	47.0	0.131	0.51231	0.51201	-3.5	1.35
Mafic dike												
SBP-12	255	419	1.761	0.71341	0.70489	9.87	48.0	0.124	0.51258	0.51231	+2.2	0.82

The decay constants used in the calculations are the values $\lambda^{87}Rb = 1.42 \times 10^{-11}$ and $\lambda^{147}Sm = 6.54 \times 10^{-12}$ $year^{-1}$ recommended by the IUGS Subcommission for Geochronology (Steiger and Jäger. 1977).

*t = time used for the calculation of the isotopic initial ratios. t = 340 Ma.

†Epsilon-Nd values were calculated relative to a chondrite present day: $(^{143}Nd/^{144}Nd)^{today}_{CHUR} = 0.512638$; $(^{143}Sm/^{144}Nd)^{today}_{CHUR} = 0.1967$.

§TDM is depleted mantle model age with average crustal Sm/Nd prior to emplacement at 340 Ma following De Paolo et al. (1991).

Table 5. Rb-Sr and Pb data for a K-feldspar crystal from the San Blas unit

Sample	Rb	Sr	$^{87}Rb/^{86}Sr$	$^{87}Sr/^{86}Sr_{(0)}$	std err%	$^{87}Sr/^{86}Sr_{(340)}$
SB1Rim	486	81	17.48	0.80429	0.0010	0.71989
SB1Core	500	83	17.56	0.80721	0.0008	0.72242
Sample	$^{206}Pb/^{204}Pb$	$^{207}Pb/^{204}Pb$	$^{208}Pb/^{204}Pb$			
SB1Rim	18.40	15.66	38.30			
SB1Core	18.80	15.98	39.10			

Table 6. Characteristics of the four magmatic fabrics in the San Blas intrusive complex

Foliation type	Orientation	Geometrical relationship to contacts between units	Intrusive units in which the fabric is preserved	Geometrical relationship to batholith/host-rock contacts	Chronology	Likely cause of magmatic fabric
Type 1	Steep (80°–90°dip), strike N-S to NNW-SSE	Unrelated	In U_A is dominant. U_{SB}, U_H	Unrelated	In U_A is the older. In U_{SB} and U_H is the last one.	Regional strain during ~WSW-ENE shortening
Type 2	Variable, parallel to nearby margins	U_A, U_{SB} and U_H parallel to contact; does not cut across the main contacts between units	U_A, U_{SB}, U_H	In U_{SB} parallel to contact	In U_A is deflected from type 1	Margin-parallel shortening caused by processes along chamber boundary
Type 3	Steep (80°–90°dip), strike E-W	Unrelated	U_{SB}, U_H In U_A is subordinate.	Unrelated	In U_{SB} and U_H overprints to type 2	Strain during N-S shortening
Type 4	sub-horizontal	Unrelated	In U_A is in contact with U_{SB}. U_{SB}, U_H	Parallel to roof contact	In U_{SB} and U_H is formed together with type 2	Roof-parallel shortening caused by processes along chamber boundary

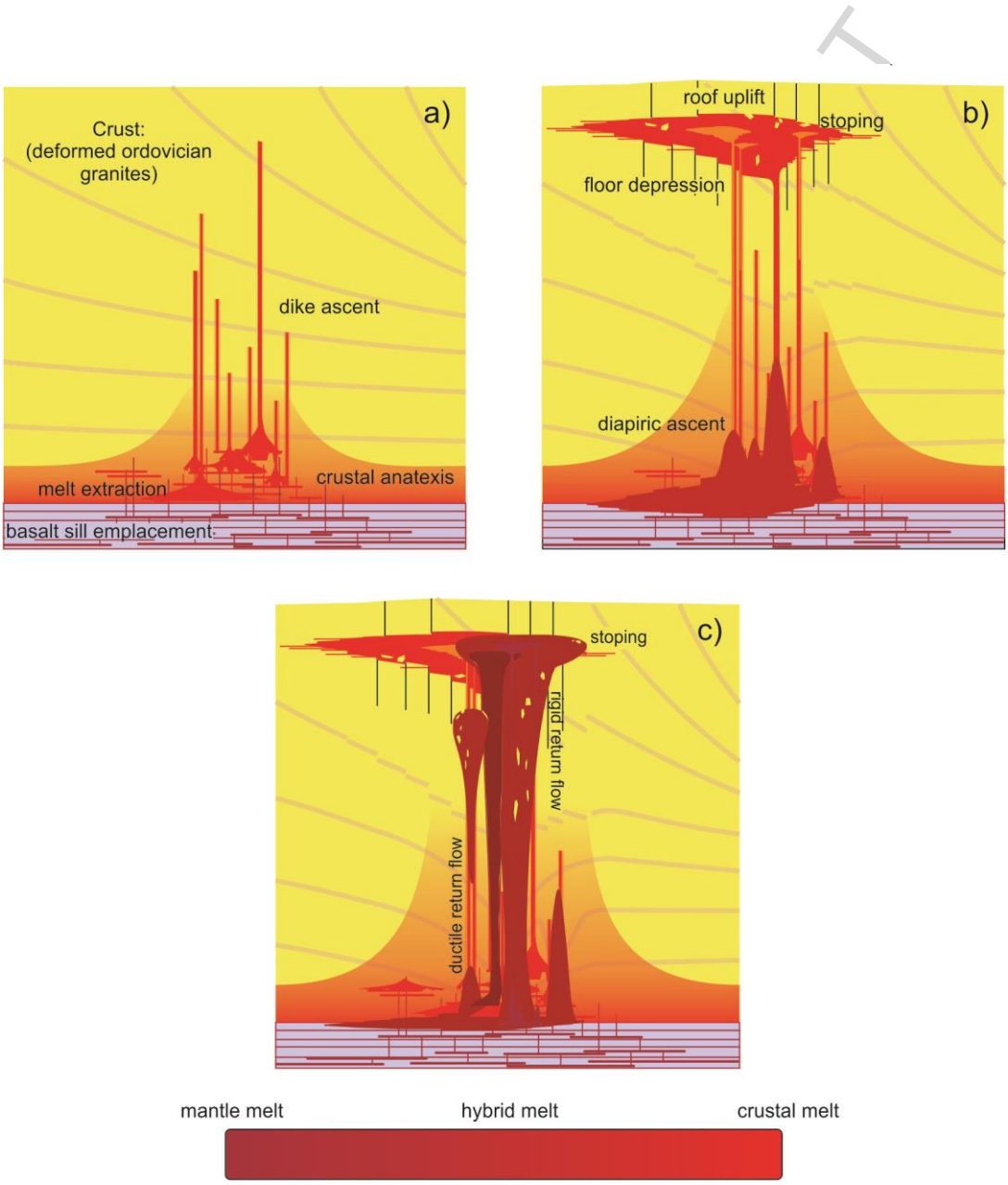

Graphical Abstract

Highlights

- The San Blas intrusive complex has variations in magma sources and emplacement style.
- Multiple magma intrusions utilize the same magmatic plumbing system.
- Such complexes may reflect the plutonic portion of polygenic volcanic centers.